

國立中央大學
National Central University

應用地質研究所
Graduate Institute of Applied Geology
碩士論文
Master Degree Thesis

菱鐵礦於高壓下電子自旋態轉變與熱傳導率之研究
Spin Transition and Thermal Conductivity of
(Fe_{0.78}Mg_{0.22}CO₃) Siderite under High Pressure

研究生：趙耕賢
Student: Keng-Hsien Chao
指導教授：黃文正博士、謝文斌博士
Advisors: Dr. Wen-Jeng Huang, Dr. Wen-Pin Hsieh

中華民國一百零七年六月
June, 2018



國立中央大學圖書館 碩博士論文電子檔授權書

本授權書授權本人撰寫之碩/博士學位論文全文電子檔(不包含紙本、詳備註 1 說明)，在「國立中央大學圖書館博碩士論文系統」。(以下請擇一勾選)

- () 同意(立即開放)
() 同意(請於西元年月日開放)
() 不同意，原因是：

在國家圖書館「臺灣博碩士論文知識加值系統」

- () 同意(立即開放)
() 同意(請於西元年月日開放)
() 不同意，原因是：

以非專屬、無償授權國立中央大學、台灣聯合大學系統圖書館與國家圖書館，基於推動「資源共享、互惠合作」之理念，於回饋社會與學術研究之目的，得不限地域、時間與次數，以紙本、微縮、光碟及其它各種方法將上列論文收錄、重製、與利用，並得將數位化之上列論文與論文電子檔以上載網路方式，提供讀者基於個人非營利性質之線上檢索、閱覽、下載或列印。

研究生簽名：趙耕賢 學號：104624012

論文名稱：菱鐵礦於高壓下電子自旋態轉變與熱傳導率之研究

指導教授姓名：黃文正，謝文斌

系所：所 博士班 碩士班

填單日期：2018/07/20

備註：

1. 本授權書之授權範圍僅限電子檔，紙本論文部分依著作權法第 15 條第 3 款之規定，採推定原則即預設同意圖書館得公開上架閱覽，如您有申請專利或投稿等考量，不同意紙本上架陳列，須另行加填申請書，詳細說明與紙本申請書下載請至本館數位博碩論文網頁。
2. 本授權書請填寫並親筆簽名後，裝訂於各紙本論文封面後之次頁（全文電子檔內之授權書簽名，可用電腦打字代替）。
3. 讀者基於個人非營利性質之線上檢索、閱覽、下載或列印上列論文，應遵守著作權法規定。

國立中央大學碩士班研究生

論文指導教授推薦書

應用地質 學系/研究所 趙耕賢 研究生所提之論
文 菱鐵礦於高壓下電子自旋態轉變與熱傳導率之研究

係由本人指導撰述，同意提付審查。

指導教授 黃文正 黃文正 (簽章)

107年 5月 16日

國立中央大學碩士班研究生
論文口試委員審定書

應用地質 研究所 趙耕賢 研究生

所提之論文

菱鐵礦於高壓下電子自旋態轉變與熱傳導率之研究

經本委員會審議，認定符合碩士資格標準。

學位考試委員會召集人

委

員

徐翰

鄭文凱

黃文正

趙耕賢

中華民國 107 年 6 月 8 日

菱鐵礦於高壓下電子自旋態轉變與熱傳導率之研究

摘 要

深層碳循環控制地球表面與內部長期的碳含量收支。該循環係由海洋板塊將碳元素隱沒至地函，而碳元素會再被火山活動循環回地表。過去研究指出，含鐵碳酸鹽，例如：菱鐵礦，是深層碳循環中重要的地函含碳礦物。此外過去研究亦指出菱鐵礦會在大約 40 GPa 至 55 GPa 發生電子自旋態轉變(由高自旋態轉變至低自旋態)並伴隨物理性質的劇烈變化，例如：彈性係數。熱傳導率為一種控制物質在兩端有溫差的狀況下，通過該物質的熱流多寡的重要物理性質，因此地球內部礦物的熱傳導率會影響其溫度構造與熱演化之過程。然而，由於過去實驗技術的困難，含鐵碳酸鹽在高溫高壓下的熱傳導率從未被研究過。本研究結合鑽石高壓砧，拉曼光譜與超快雷射技術(Time-domain thermoreflectance)，測量菱鐵礦從常壓至 67 GPa 的熱傳導率變化。我們發現菱鐵礦的熱傳導率在電子自旋態轉變的壓力範圍內會發生劇烈的變化：當菱鐵礦所受之壓力介於 40 GPa 至 55 GPa 之間且低自旋態鐵的比例估計介於 50%至 85%之間時，熱傳導率會劇烈地增加三倍；在電子自旋態轉變幾乎結束時，熱傳導率會下降至最高值的 1/9。這種在小壓力範圍內發生的劇烈熱傳導率變化意謂著如果菱鐵礦可以被板塊隱沒至 1100 至 1500 公里深，則可能會產生局部的熱流以及溫度異常，進一步影響局部礦物相的穩定度。

Spin transition and thermal conductivity of (Fe_{0.78}Mg_{0.22}CO₃) siderite under high pressure

ABSTRACT

Deep carbon cycle is a cycle controlling the long-term budget of carbon on Earth's surface and in Earth's interior: the carbon is transported to the mantle by the subduction of slabs and recycled back to the Earth's surface by the volcanic activities, respectively. Iron-bearing carbonate, for example, siderite, was proposed to be an important mantle carbon-hosting mineral in the deep carbon cycle. Previous literature showed that the siderite undergoes a pressure-induced iron spin transition (from high spin to low spin) around 40-55 GPa and the physical properties of siderite, such as elastic properties, change drastically across the spin transition. The thermal conductivity is a critical physical property that controls the heat flux flowing through a mineral when temperature gradient exists, and therefore, thermal conductivity controls the temperature profile and thermal structure evolution in Earth's interior. However, the thermal conductivity of iron-bearing carbonate has never been investigated under relevant extreme temperature and pressure conditions due to the experimental difficulties. In this work, we combined the diamond anvil cell, Raman spectroscopy and time-domain thermoreflectance techniques to measure the thermal conductivity of siderite from ambient condition to 67 GPa, in particular across the spin transition. We found that the thermal conductivity varies drastically across the spin transition: when siderite is under 40-55 GPa, the thermal conductivity increases by three times as the fraction of low spin iron is estimated to be around 50-85% and suddenly drops to around 1/9 of its maximum value as the spin transition almost completes. These results imply that if the siderite could be transported to the depth of 1100-1500 km by the subduction of slabs, the thermal conductivity anomaly of siderite that varies drastically within a narrow pressure range might induce local heat flux and temperature anomalies, and therefore, influence the stability of local mineral phases.

ACKNOWLEDGMENT

This thesis is instructed and guided by Dr. Wen-Jeng Owen Huang in National Central University and Dr. Wen-Pin Hsieh in Academia Sinica. I would like to express my deepest appreciations to two advisors.

Dr. Huang found my potent and zeal in the mineral field since I was freshman at the National Central University. After I became graduate student, Dr. Huang recommended me to study advanced knowledge in Dr. Hsieh's group.

I very appreciate Dr. Hsieh's guide and training in his group. Dr. Hsieh not merely trained me but he is also always glad to discuss with me whenever I have new discovery. He will not always give me an answer immediately, instead, I was trained to speculate and find the answer by myself. Thus, I can remember the knowledge for longer.

I would also like to express my thankfulness to other members of my group, Mr. Chao-Chih George Chen, Mr. Yu-Hsiang Vincent Chien, and Miss. Yun-Yuan Chang. Mr. Chen thought me the basic set up of diamond anvil cell and the operation of instruments such as TDTR. Mr. Chien and Dr. Chang frequently gave me advice and questioned me about some potential logical loopholes of this thesis, making this study more convincing.

I would also like to thanks Dr. Jennifer Kung, Mr. Sheng-Chih Chuang in Department of Earth Sciences, National Cheng-Kung University for helping me detect the orientation of siderite sample and Dr. Yoshiyuki Iizuka in Institute of Earth Science Academia Sinica for helping me determine the precise chemical composition of siderite sample.

Finally, I would like to express my appreciations to my parents. They have provided me the financial and spiritual aids for 25 years. Therefore, I would like to dedicate this achievement to my parents.

TABLE OF CONTENTS

CHINESES ABSTRACT.....	i
ENGLISH ABSTRACT.....	ii
ACKNOWLEDGMENT.....	iii
TABLE OF CONTENTS.....	iv
LIST OF FIGURES.....	vi
LIST OF TABLES.....	vii
LIST OF SYMBOLS.....	viii
CHAPTER 1: INTRODUCTION.....	1
1.1. Deep carbon cycle.....	1
1.2. Pressure-induced iron spin transition in siderite.....	3
1.3. Structure of siderite (calcite-group rhombohedral carbonate)	5
1.4. Review of techniques measuring thermal conductivity at high pressure.....	7
1.5. Motivations and scientific goals.....	11
CHAPTER 2: EXPERIMENTAL METHODS.....	13
2.1. Sample preparation and characterization.....	13
2.1.1. Sample preparation.....	13
2.1.2. Characterization of the sample composition by electron micro probe analyzer (EPMA).....	13
2.1.3. Determination of the crystal orientation by electron backscattered diffraction (EBSD).....	15
2.1.4. Determination of the crystal orientation by Laue diffraction.....	18
2.2. Raman spectroscopy.....	21
2.2.1. Principle of Raman spectroscopy.....	21
2.2.2. Spin state characterization by Raman spectroscopy.....	23
2.2.3. Comparison of experimental methods characterizing the spin state of siderite.....	27
2.3. High-pressure experimental setup.....	30
2.4. Time-domain thermoreflectance (TDTR).....	33
2.5. Thermal model and parameters in the TDTR analysis.....	36
2.5.1. Configuration of the thermal model.....	36
2.5.2. Thermal conductivity and heat capacity of the silicone oil layer.....	37
2.5.3. Thermal conductivity and heat capacity of the aluminum layer.....	38
2.5.4. Thickness of aluminum layer.....	39
2.5.5. Heat capacity of siderite.....	46
2.5.6. Thermal conductance of interfaces.....	47

2.5.7. Deriving thermal conductivity of sample.	47
CHAPTER 3: RESULTS AND DISCUSSION.	49
3.1. Raman spectra of siderite.	49
3.2. Results of thermal conductivity along <i>a</i> -axis.	56
3.3. Results of thermal conductivity along <i>c</i> -axis.	61
3.4. Uncertainties of TDTR.	66
CHAPTER 4: SUMMARY.	78
REFERENCES.	80

LIST OF FIGURES

Figure 1. Atomic structures of the calcite-group minerals.	7
Figure 2. Kikuchi bands of <i>a</i> -axis obtained from the EBSD experiment	16
Figure 3. Failed confirmation of <i>c</i> -axis by EBSD	17
Figure 4. Raw data of Laue-diffraction pattern of <i>c</i> -axis	20
Figure 5. Picked points from the Laue-diffraction pattern of <i>c</i> -axis.	20
Figure 6. The confirmation of <i>c</i> -axis by Laue-diffraction.	21
Figure 7. Characterization of fraction of low spin iron by Raman spectrum	26
Figure 8. Setup of diamond anvil cell.	30
Figure 9. Pressure derived from hydrostatic and non-hydrostatic equations	33
Figure 10. Setup of TDTR	35
Figure 11. Schematic drawing of thermal model.	36
Figure 12. Lattice parameters of siderite as a function of pressure.	43
Figure 13. Example data of ratio as a function of delay time under 1.39 GPa.	48
Figure 14. Raman spectra of siderite and silicone oil before compression.	50
Figure 15. Representative Raman spectra of the siderite during compression and decompression cycles.	51
Figure 16. The pressure range of spin transition in several studies.	52
Figure 17. Distance between cations in several forms of metal polyhedra connection arrangements.	55
Figure 18. Thermal conductivity of siderite as a function of pressure along <i>a</i> -axis during compression	58
Figure 19. Damaged aluminum layer under 35 GPa	60
Figure 20. Pressure dependence of the thermal conductivity of siderite along <i>c</i> -axis.	61
Figure 21. Inhomogeneous thermal conductivity caused by the spatially inhomogeneous distribution of spin state	62
Figure 22. Thermal conductivity of siderite as a function of Normalized $A_{v_1}^{LS} / (A_{v_1}^{LS} + A_{v_1}^{HS})$	63
Figure 23. Estimation of error bars of Normalized $A_{v_1}^{LS} / (A_{v_1}^{LS} + A_{v_1}^{HS})$	65
Figure 24. Process to figure out the sensitivity parameters under ambient condition	68
Figure 25. Sensitivity parameters under several pressures.	69

LIST OF TABLES

Table 1. EPMA data of siderite in this study.	15
Table 2. Comparison of several experimental methods used to characterize the spin state of iron in siderite.	29
Table 3. Lattice parameters and volume of the unit cell of siderite from 0.4 to 60 GPa.	41
Table 4. Averaged sensitivity parameters contributed by parameters of thermal model.	76
Table 5. Estimated errors contributed by the sensitivity parameters of thermal model.	77

LIST OF SYMBOLS

- P : Pressure
- a : Lattice parameter along a -axis
- b : Lattice parameter along b -axis
- c : Lattice parameter along c -axis
- T : Translational mode of carbonate ions
- L : Librational mode of carbonate ions
- ν_1 : In-plane bending mode of carbonate ions
- ν_4 : Symmetric stretching mode of carbonate ions
- R_1 : The standard peak of ruby fluorescence
- λ_0 : Wavelength of R_1 peak under ambient condition
- λ : Wavelength of R_1 peak under high-pressure
- V_{in} : In-phase voltage
- V_{out} : Out-phase voltage
- C : Volumetric heat capacity
- C_{si} : Volumetric heat capacity of silicone oil
- C_{Al} : Volumetric heat capacity of aluminum
- $C_{sid.}$: Volumetric heat capacity of siderite
- A : Thermal conductivity
- A_{Si} : Thermal conductivity of silicone oil
- A_{Al} : Thermal conductivity of aluminum
- $A_{Sid.}$: Thermal conductivity of siderite
- e : Thermal effusivity
- e_{Si} : Thermal effusivity of silicone oil
- e_{Al} : Thermal effusivity of aluminum
- $e_{Sid.}$: Thermal effusivity of siderite
- G : Thermal conductance of materials interface
- G_1 : Thermal conductance of silicone oil-aluminum interface
- G_2 : Thermal conductance of aluminum-siderite interface
- h_{Al} : Thickness of aluminum film
- ρ_{Al} : Density of aluminum

CHAPTER 1

INTRODUCTION

1.1. Deep carbon cycle

Deep carbon cycle is a cycling process carrying carbon on Earth's surface into Earth's interior and returning to the surface. It is believed that carbon is transported into the mantle by the subduction of slabs and recycled back to the surface by volcanic activities, respectively. Carbon typically exists in subduction slabs in two forms: carbonate sediments created by marine creatures and carbonated peridotite formed from the reaction between carbon dioxide and olivine-rich oceanic plates, respectively. The carbonate sediments are estimated to form 1/3 of the total amount of carbon transported into the mantle, and the carbonated peridotite is estimated to form the remaining 2/3 [1]. The volcanic activities can recycle the carbon back to the surface, yet, the precise amount of carbon recycled back to the surface by volcanic activities requires further investigations. The mechanisms of deep carbon cycle and calculations of carbon flux in detail can be found in Dasgupta and Hirschmann [1].

Deep carbon cycle controls the long-term carbon budget of Earth's surface and interior [1]. Therefore, there have been plenty of studies focusing on the carbon-bearing materials in the mantle since the 1990s. The most common study is to focus on finding the potential carbon hosting candidates in the mantle and investigating

their physical properties under high-pressure and high-temperature conditions.

Magnesite, a carbonate mineral being stable under lower mantle condition [2, 3], was suggested to be an important carbon hosting mineral in Earth's interior in early studies [4]. Fe-bearing carbonate, e.g., siderite, has been recently suggested to be another candidate carbon hosting mineral in the lower part of the mantle [5-7], and its physical properties, including elastic constants [8], equation of state [9], and optical properties [7], under high-pressure conditions have been extensively studied in the past few years. In particular, a transition of electronic spin state (from high-spin to low-spin) was observed between 40-55 GPa, where the color and sound velocity of siderite change accordingly.

Thermal conductivity is a key factor controlling the heat flux flowing through a material when a temperature gradient exists, and thus, the thermal conductivity of minerals influences the temperature distribution in Earth's interior. The temperature distribution will further influence the stability of mineral phases, which in turn controls the forms of minerals in Earth's interior. Although many physical properties of siderite have been extensively studied in order to understand the deep carbon cycle, due to experimental difficulties, the thermal conductivity that holds a key to determine the thermal structure and dynamics in the deep carbon cycle has never been investigated under relevant pressure and temperature. In this work, we investigated

the thermal conductivity of siderite from ambient condition to 67 GPa at room temperature.

1.2. Pressure-induced iron spin transition in siderite

Iron is the most common transition metal in Earth's interior, where the pressure is extremely high. The high pressure can make iron undergo spin transition, and therefore, the pressure-induced iron spin transition is a common phenomenon that has been observed in lower mantle minerals. The mechanism of pressure-induced iron spin transition is shown as below.

There are six and five valence electrons in the $3d$ orbitals of Fe^{2+} and Fe^{3+} , respectively. Normally, these six or five electrons occupy five $3d$ orbitals (d_z^2 , $d_{x^2-y^2}$, d_{xy} , d_{yz} , d_{xz}) and the energy level of these five orbitals are almost the same. These electrons fill into the five d orbitals by following the Hund's rules and maintain greatest total spin of the whole iron atom. However, when iron forms the minerals, several anions surround the iron and form a polyhedron within mineral's structure (oxygen is the most common anion combining with iron to form minerals in Earth's mantle). Due to the negative charge of the anion, some orbitals closing to the direction of anion are repulsed by the negative charges and their energy level increases. This repulsive force makes the d orbitals split into several groups with slightly different

energy levels and the split energy depends on the shapes of polyhedra and the distance between the orbital and the anion. For example, in the siderite, the oxygen and iron form the octahedron, and therefore, the d orbitals split into two energy levels termed e_g and t_{2g} . The e_g of iron of siderite contains two orbitals, the d_z^2 and $d_{x^2-y^2}$, which face to the oxygen directly and they are repulsed by the oxygen most intensely; the t_{2g} of iron of siderite contains three orbitals, the d_{xy} , d_{yz} and d_{xz} , which do not face the oxygen directly, and these orbitals are less repulsed.

If an iron-bearing mineral is under relatively low pressure, the energy gap within the split d orbitals is not so great and the relatively low energy gap allows the valence electrons to follow the Hund's rule to occupy all of the d orbitals to maintain greatest total spin of an atom; however, when pressure increases to certain degree, the repulsive force between anion and d orbitals will make the energy gap within split d orbitals become too great to allow the valence electrons to follow the Hund's rule, and thus, the electrons are forced to be filled into the relatively low energy level orbitals and in turn forced to pair with each other. This phenomenon is termed pressure-induced spin transition. For instance, when the siderite is under relatively low pressure, the energy gap between e_g and t_{2g} is not so great, and thus, the valence electrons of iron can still occupy five d orbitals by following the Hund's rules and maintain greatest total spin of the whole atom; when siderite is compressed to 40-55

GPa, the distance between oxygen and iron is compressed and the increasing repulsive force from the oxygen makes the energy gap between the e_g and t_{2g} become too great to allow the electrons following the Hund's rule. Consequently, the valence electrons of iron are forced to pair each other into the t_{2g} when siderite is compressed to 40-55 GPa. The more details of several types of pressure-induced spin transitions in Earth's interior can be found in Lin and Wheat [10]. In this study, we used Raman spectroscopy to characterize the spin state of siderite. The principle to characterize the spin state by Raman spectroscopy can be found in **section 2.2.1-2.2.2**.

1.3. Structure of siderite (calcite-group rhombohedral carbonate)

Siderite is the iron end member of calcite-group rhombohedral carbonate. Its structure is the calcite-group rhombohedral carbonate structure that can be envisioned as a distorted halite (rock salt) structure (**Fig. 1**). One can obtain the calcite-group rhombohedral structure by squeezing the cubic halite crystal along [111] and replacing the sodium and the chlorine with calcium and carbonate groups, respectively. The only difference between calcite and siderite is to replace calcium with iron again.

Every calcite-group rhombohedral carbonate has the same space-group symmetry, $R\bar{3}C$. There are three categories of commonly used unit cells for calcite-group minerals. The trigonal system rhombohedral cell contains two units of XCO_3 ($X = Ca^{2+}, Mg^{2+}, Fe^{2+}, Mn^{2+}$), the most commonly used rhombohedral cell comprises four units of XCO_3 , and the hexagonal cell consists of six units of XCO_3 in a unit cell determined by a, b, c of three axes [11]; in the hexagonal cell, although the length of a equals to the length of b , mineralogists typically separate a and b to follow a standard: all of the lattice parameters are expressed as a, b, c regardless to their length and their crystal system. The siderite unit cell in this study is based on the hexagonal cell which contains a, b, c three lattice parameters, because the methods used to characterize the crystal orientation in this study, for example, electron backscattered diffraction and Laue diffraction, are based on the hexagonal cell.

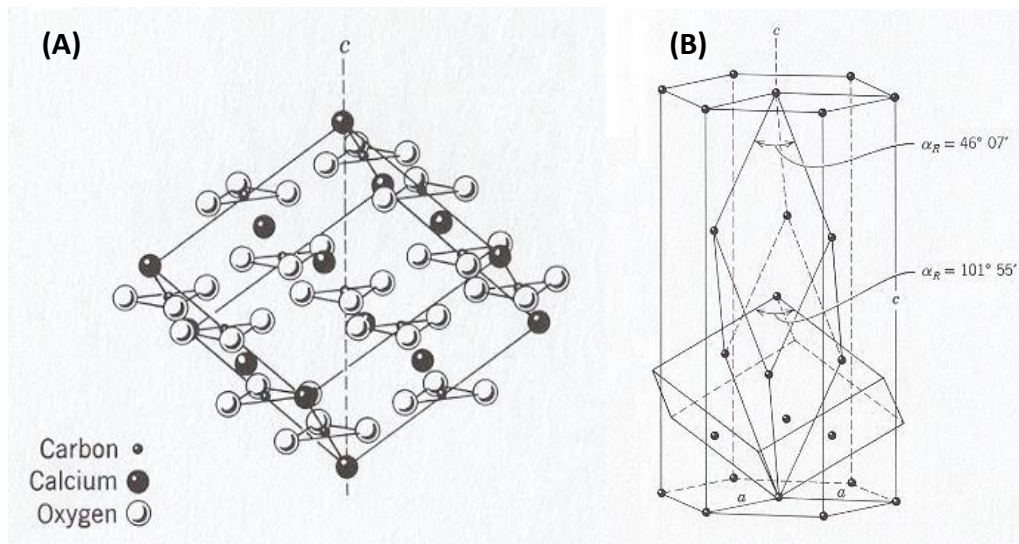


Figure 1. Atomic structures of the calcite-group minerals. (A) The composition and relative location of atoms in the typically used calcite structure. In this conventional structure, the eight corners and six face centers are occupied by calcium ions. Body center and the middle point of each side are occupied by the carbonate groups. (B) Several categories of the unit cell to determine the calcite structure: the slender trigonal system rhombohedral cell, the typical rhombohedral cell as the figure in the left-hand-side, and the hexagonal cell determined by a , b , c three axes. Both figures are cited from Manual of Mineralogy [11].

1.4. Review of techniques measuring thermal conductivity at high pressure

Thermal properties (e.g. thermal conductivity) of geological materials at high pressure has been studied for nearly a century. Early in the 1920s, in order to study the thermal structure within the Earth, Percy Williams Bridgman pointed out the importance to measure the thermal properties of rocks under high pressure [12]. However, being restricted to contemporary experimental techniques, the pressure achievable in Brigman's study was only around 1 GPa, where the changes in thermal properties of most materials were minor. Before the 1960s, the pressure was generated

by piston-cylinder apparatus and the pressure achievable was low. For example, the pressure generated by piston-cylinder apparatus in 1960 was around 5 GPa [13].

As the technology of high pressure generating devices was improved from the 1960s to 1990s, scientists managed to study thermal conductivity at much higher pressure by measuring the thermal conductivity of material within a multi-anvil apparatus with Å ngström method [14-16]. In the Å ngström method, a heater surrounding a cylindrical sample heats the sample by a sinusoidal temperature wave and the heat propagates into sample radially, generating a sine curve temperature distribution in the sample. Typically, the higher the thermal diffusivity is, the higher the amplitude and the frequency of temperature curve are, and therefore, the thermal conductivity, which is associated with thermal diffusivity, can be derived. However, generally speaking, the current limitation of pressure generated by the multi-anvil apparatus is typically around 30 GPa. Gem anvil cell, e.g. diamond anvil cell (DAC), can generate higher pressure than the multi-anvil cell. For example, a well-designed diamond anvil cell can generate pressure up to 750 GPa [17], yet, diamond anvil cell has problems to be compatible with aforementioned contemporary thermal property measuring methods, however. This is because, in the aforementioned methods, such as Å ngström method, the heating apparatus and thermal couples must be connected with wires to heat the sample and to measure the temperature, yet, there are

difficulties to set up wires within the DAC due to the narrow space in the DAC (the sample chamber is only around 50-500 μm -wide). Even one successfully sets up wires in the DAC, the wires are easy to short-circuit due to the space narrowness between wires or burnout during the heating progress due to their thinness.

In the early twenty-first century, a new method, optical pulsed transient heating method, was introduced to measure thermal conductivity of material under high pressure [18]. In this method, a thin metallic coupler is embedded in the sample. The metallic coupler is heated by a pulsed laser and the heat diffuses into the surrounding sample. Typically, the higher the thermal diffusivity of the sample is, the shorter the cooling time of metallic coupler is. The thermal diffusivity of the sample is derived by measuring the cooling rate of the coupler by finite element model.

However, some factors that cannot be ignored may contribute error to the result and decrease its accuracy. For instance, the laser energy absorption in the metallic coupler may reduce the surface temperature of the coupler and this absorption is not considered in the model calculation, causing an error which is typically greater than 50%. Another disadvantage of the optical pulsed transient heating method is that, due to its reliance on the intensity of black-body radiation spectrum, the sample must be above a certain temperature; thus its working temperature is typically restricted to not lower than ≈ 1400 K.

Time-domain thermoreflectance (TDTR) is an ultrafast optical method used to study thermal conductivity in the material science field under ambient condition.

Although this method was typically utilized to measure the thermal conductivity of material or thermal conductance of interface between two materials under room pressure and room temperature, after 2009, Dr. Wen-Pin Hsieh and his colleagues [19-21] combined TDTR with the diamond anvil cell to measure thermal conductivity of materials at high pressure. After Dr. Wen-Pin Hsieh returned to Taiwan and hosted our lab, this method was also introduced to Taiwan, allowing our team to study the thermal conductivity of minerals accurately at relevant pressure range. In the setup of TDTR, the laser is split to pump and probe beams; the pump beam heats a metal film coated on the sample while the probe beam measures the reflectivity change of the metal film, which is associated with the cooling rate of metal film. The thermal conductivity of the sample is extracted by calculating the reflectivity (temperature) variation in our thermal model. The uncertainty of TDTR is generally less than 10% under ambient condition and increases to around 25% under high-pressure condition.

Its accuracy and convenience are superior to the optical pulsed transient heating method.

1.5. Motivations and scientific goals

Thermal conductivity is a critical factor controlling the heat flux and temperature profile in Earth's interior, and therefore, it influences the stability of mineral phases and thermal structure evolution in Earth's interior. For example, according to Chang et al. [22], the thermal conductivity of hydrous olivine covering the slabs is only half of the thermal conductivity of anhydrous olivine as pressure becomes greater than 5 GPa. This low-thermal-conductivity hydrous olivine will prevent the slabs from being heated by the surrounding high-temperature mantle, and thus, decreases the temperature in the center of slabs, allowing metastable olivine in slabs' center to survive to the deeper depth.

Siderite is an important lower mantle carbon hosting candidate in the deep carbon cycle, yet, the lattice thermal conductivity of siderite under extreme pressure and temperature has never been investigated due to previous experimental difficulties. Therefore, in this work, we combined the diamond anvil cell, Raman spectroscopy, and TDTR to investigate the thermal conductivity of the natural siderite sample along *a*-axis and *c*-axis up to 67 GPa to discuss potential impact in the lower mantle caused by the spin transition of siderite. We found that there is a thermal conductivity anomaly at the pressure range of spin transition, 40-55 GPa: the thermal conductivity of siderite drastically increases as the fraction of low spin iron increases and drops as

spin transition almost completes. This thermal conductivity anomaly may generate local temperature anomaly in the mantle and influence the stability of local mineral phases; such anomalies of temperature profile or anomalies of stability of mineral phases may become new factors or potential uncertainties that the previous scientists studying the thermal structure of mantle has never considered.

CHAPTER 2

EXPERIMENTAL METHODS

2.1. Sample preparation and characterization

2.1.1. Sample preparation

Siderite samples from Iouriren Mine, Akka, Tafreout, Tiznit Province, Souss-Massa-Praa Region, Morocco was used in this study. We broke the samples into several rhombohedral single crystal fragments along its well-developed cleavages. Siderite fragments were polished down to a thickness less than 25 μm along the *a*-axis and *c*-axis and then coated with aluminum films with around 90 nm-thickness by a thermal evaporator. After the samples were coated with aluminum films, we typically cut the samples into a size of 45-90 \times 45-90 μm . This sample size allowed us to load the sample into the diamond anvil cell with a 120 μm -diameter hole rhenium gasket and allowed us to collect more than two data points by the 14 μm -diameter beam of TDTR system.

2.1.2. Characterization of the sample composition by electron micro probe analyzer (EPMA)

We commissioned our siderite samples to Dr. Yoshiyuki Iizuka in Electron Probe Micro-Analyses Lab, Academia Sinica to measure the precise composition of

siderite. The basic principle of EPMA is to bombard the sample with an electron beam and obtain the fingerprints of elements from emitted X-ray. Once the beam hits the electrons in the inner shells of an atom, it removes the electron in the inner shells and creates a vacancy. Then the remained electrons occupying the outer shells drop into this vacancy and emit X-ray. Thus, we can obtain the chemical composition by analyzing the characteristics of X-ray. For instance, the frequency of X-ray reflects the energy level of shells, which is associated with the categories of elements, and the intensity of emitted X-ray is associated with the proportion of certain elements in the sample. The more details of EPMA technology can be found in Reed [23]. The composition of our siderite sample measured by the EPMA is shown in **Table. 1**. We determine the composition to be $\text{Fe}_{0.78}\text{Mg}_{0.22}\text{CO}_3$.

Sample No.	Mass percentage				Metal cation fraction (Total O = 3.0)			
	MgO	FeO	MnO	Total	Mg	Fe	Mn	Total
1	8.506	54.761	2.012	65.437	0.2157	0.7789	0.0290	1.0265
2	8.475	54.728	2.018	65.456	0.2192	0.7940	0.0296	1.0472
3	8.567	54.799	1.914	65.539	0.2188	0.7852	0.0278	1.0365
4	8.507	54.845	2.140	65.679	0.2169	0.7844	0.0310	1.0357
5	8.570	54.802	1.904	65.467	0.2160	0.7747	0.0273	1.0215
6	8.353	54.470	2.062	65.142	0.2113	0.7731	0.0296	1.0187
7	8.870	54.484	1.805	65.335	0.2283	0.7866	0.0264	1.0446
8	9.263	54.398	1.847	65.715	0.2350	0.7744	0.0266	1.0398
Minimum	8.353	54.398	1.805	65.142	0.2113	0.7731	0.0264	1.0187
Maximum	9.263	54.845	2.140	65.715	0.2350	0.7940	0.0310	1.0472
Average	8.639	54.661	1.963	65.471	0.2201	0.7814	0.0284	1.0338
Standard deviation	0.292	0.179	0.114	0.183	0.0077	0.0074	0.0016	0.0105

Table 1. EPMA data of siderite in this study. In the left-hand panel, each row of the first column represents the sampling number, the minimum value, maximum value, average and the standard deviation from up to down. The second to the fourth columns are the mass percentage of oxide in siderite except for the CO₂. The “total” in the fifth column is the sum of the mass percentage over the former three columns. The right-hand panel shows the fraction of metal in a chemical formula Fe_xMg_yMn_zCO₃ and $x+y+z=1$. We find that the amount of Mn is almost negligible in this characterization. Therefore, we determine the composition of siderite to be Fe_{0.78}Mg_{0.22}CO₃.

2.1.3. Determination of the crystal orientation by electron backscattered diffraction (EBSD)

We commissioned our siderite samples to Miss Yu-Chieh Lin in Field Emission Scanning Electron Microscopy Lab, National Taiwan University, to help us confirm the axis direction of our sample by the EBSD. The sample was tilted to 70 degrees in a normal scanning electron microscope (SEM). The electrons emitted from the SEM hit the sample and were backscattered to the Charge Coupled Device (CCD).

The backscattered diffraction pattern depends on the arrangement of atoms within the sample, and thus, the direction of the crystal is determined. The more details of EBSD technology can be found in Randle [24]

The EBSD system determines the orientation of crystal by fitting the backscattered pattern called Kikuchi bands [25]. In this measurement, the sample with orientation along the a -axis (100) was successfully confirmed (**Fig. 2**), and therefore siderite sample with a -axis along its plane normal was coated with an aluminum film and used to investigate the thermal conductivity along a -axis. We will discuss the results of thermal conductivity of this a -axis upward siderite in **section 3.5**.

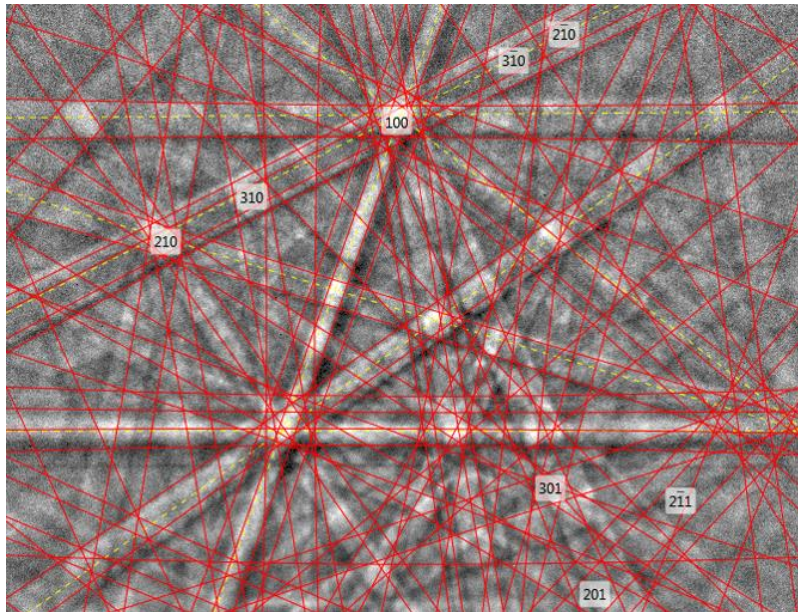


Figure 2. Kikuchi bands of a -axis obtained from the EBSD experiment. The Miller index of a -axis of siderite is supposed to be (100) in the EBSD system, and the (100) does appear. Although the (100) is not in the middle part of the image, the tilted angle is minor. Thus, the surface of the sample is confirmed to be mostly along the a -axis.

However, we failed to confirm the orientation along c -axis (**Fig. 3**). The correct Miller index of c -axis is supposed to be (001), yet, in **Fig. 3**, the Miller index of the face is (111). We suspected this pattern was misinterpreted due to the lack of accurate lattice parameters in the database. This is because we need accurate lattice parameters of crystal to help us fit the Kikuchi bands and characterize the orientation of crystal. The data of siderite from the database of Field Emission Scanning Electron Microscopy Lab, National Taiwan University is based on pure FeCO_3 ; however, our sample contains magnesium which changes the lattice parameters. Consequently, the database gave a false interpretation.

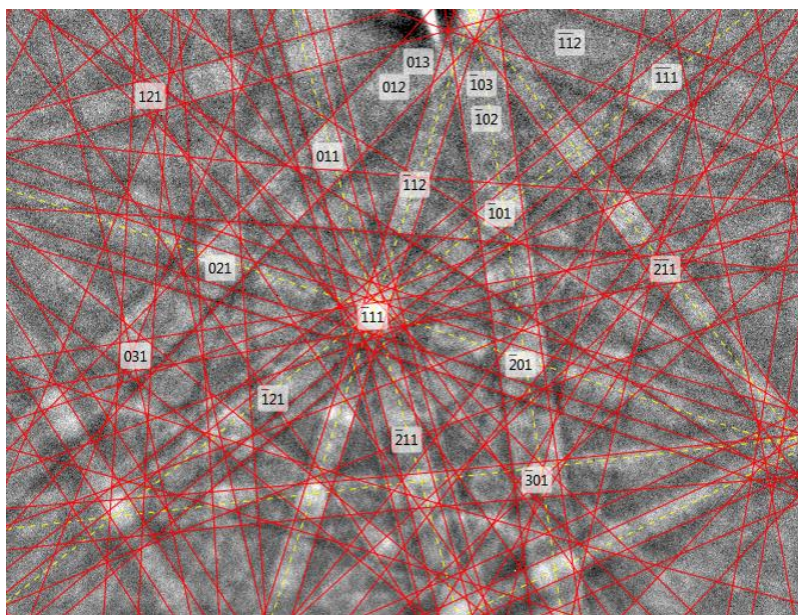


Figure 3. Failed confirmation of c -axis by EBSD. The Kikuchi bands show that the orientation of the surface is (111), rather than the expected orientation of (001).

Another problem we engaged is that the clearness of Kikuchi bands highly depends on the flatness of sample. Typically, the flatter the sample surface is, the

clearer the Kikuchi bands are. However, it is difficult to control the flatness of a sample surface. Unfortunately, we never got any usable information after second time EBSD experiment. The patterns of Kikuchi bands have never been clear enough to let us confirm the crystal orientation since our second-time experiment, leading to the wrong interpretation. To overcome the orientation confirmation problem, we chose the Laue diffraction to help us to cross-check the crystal orientation.

2.1.4. Determination of the crystal orientation by Laue diffraction

We need flat samples to get clear differential pattern by the EBSD, yet, the flatness to get high-quality data from the EBSD is extremely strict and difficult to control. We spent plenty of time polishing the sample, the EBSD experiment did not necessarily provide clear differential patterns or desirable data every time. Prof. Jennifer Kung and Mr. Sheng-Chih Chuang in Mineral and Rock Physics Laboratory, National Cheng-Kung University, kindly helped characterize the crystal orientation of our siderite samples. There is no strict flatness limitation of sample surface if we measure the crystal orientation by the Laue diffraction. Therefore, the crystal orientation of our siderite samples along *c*-axis was characterized by Laue diffraction, which can offer more reliable and reproducible results within shorter time.

Laue diffraction is a kind of X-ray diffraction method, yet it is slightly different from the commonly used X-ray diffraction. The commonly used X-ray diffraction system utilizes monochromatic (single wavelength) X-ray and rotates the orientation of samples to obtain the information of atomic arrangements, whereas the Laue diffraction system utilizes polychromatic (multiple wavelengths) X-ray to measure the structure of samples without rotating the crystal orientation of samples. Thus, by fitting the Laue diffraction pattern with a pattern of a known structure along a certain direction, we can obtain the direction of a crystal.

Since the confirmation along *c*-axis failed in the EBSD experiments, we mostly desired to confirm the direction of *c*-axis of sample to continue our study and we successfully confirmed that the crystal was along *c*-axis this time. The results are shown below (**Figs. 4-6**).

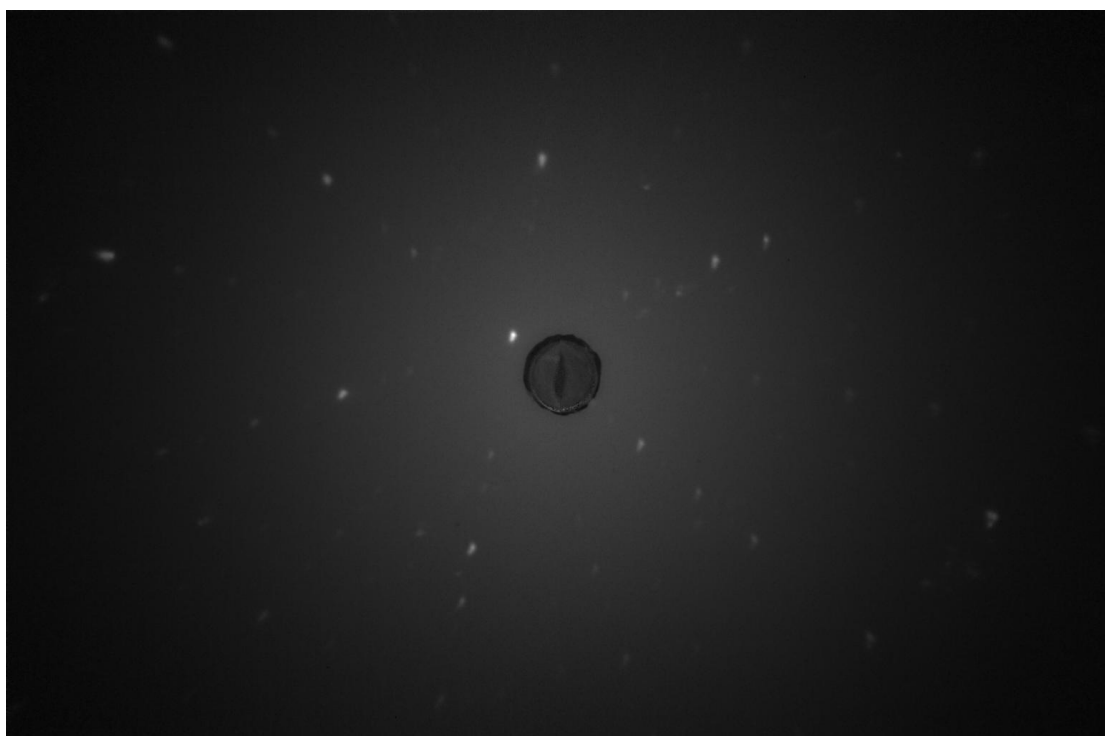


Figure 4. Raw data of Laue-diffraction pattern of c -axis.



Figure 5. Picked points from the Laue-diffraction pattern of c -axis.

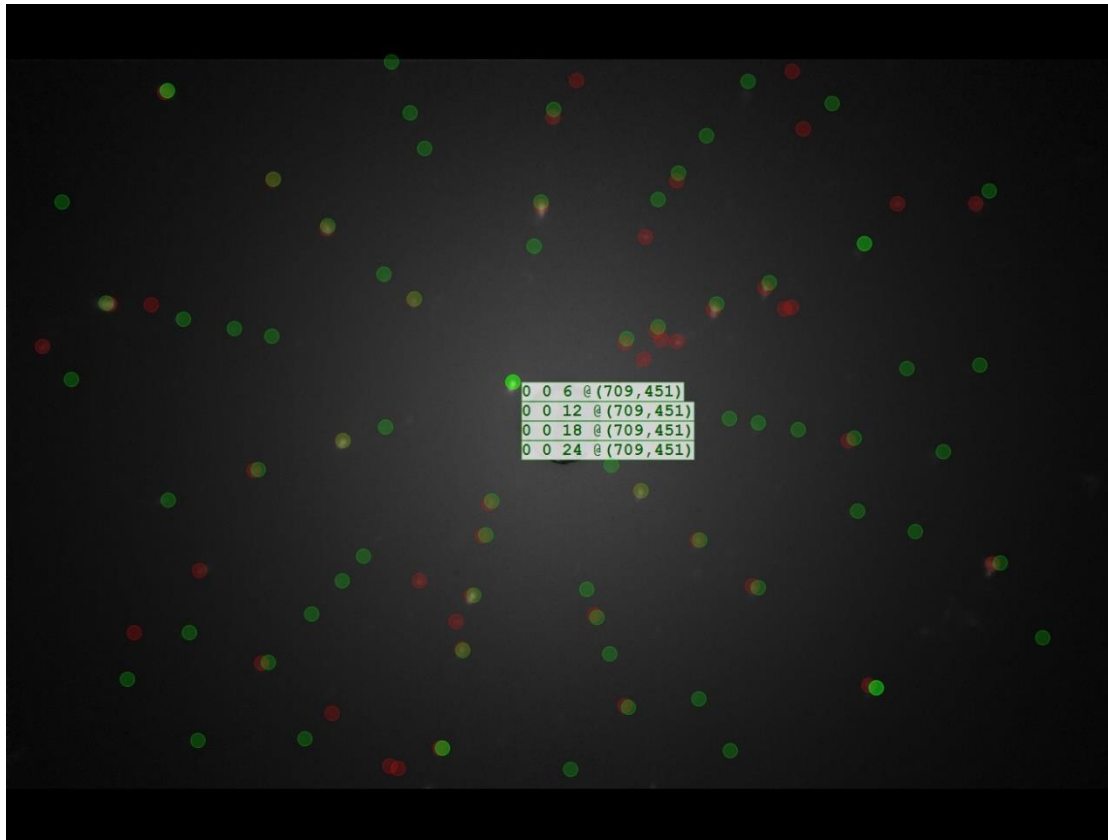


Figure 6. The confirmation of *c*-axis by Laue-diffraction. The green spots are the known pattern used to fit the red spots. The orientation of the surface plane is shown in the middle part of the screen with Miller index. Although the Miller index of *c*-axis typically expressed as (001), the number in the image such as (006) is equivalent to (001).

According to the three figures, **Figs. 4-6** above, we confirmed that this time, the orientation of our sample was along *c*-axis, and the sample was coated with an aluminum film for thermal conductivity measurements by the TDTR.

2.2. Raman spectroscopy

2.2.1. Principle of Raman spectroscopy

Raman spectroscopy is an optical technique to study vibrations of chemical bonds in a material. The principle of Raman spectroscopy is that incident photons

interact with phonons and the photons are scattered once the material is irradiated by the light. Most of the photons are elastically scattered without changing their original frequency, known as Rayleigh scattering. However, around 10^{-5} - 10^{-9} of scattered photons may slightly change their frequency due to the inelastic scattering. This phenomenon is termed Raman scattering, which was discovered by the Indian scientist, Raman [26]. The frequency and/or wavenumber of Raman scattered photons contains the information of phonons, which is associated with the vibrational information of chemical bonds, such as vibrational frequency and the geometry of bonds, allowing us to study the vibration modes of chemical bonds in the sample.

In this research, we used Raman spectroscopy to detect the vibrational spectra of siderite and identify its electronic spin state. In a Raman spectrum of siderite, there are four major vibrational modes below 1200 cm^{-1} wavenumber. These are the common peaks of the calcite group minerals. Two of them are external modes locating at around 154 cm^{-1} and 280 cm^{-1} , respectively. The external modes can be considered as the collective motion of molecules as a whole. For example, the mode locating at 280 cm^{-1} is the translator oscillation of a CO_3 group and the neighboring CO_3 groups in the same layer will also vibrate along the same direction in the same time, and thus, this vibration occurring in the whole layer of CO_3 groups is termed external mode. Other two modes are internal modes locating at 712 cm^{-1} and 1086 cm^{-1} .

¹, respectively. The internal mode means that the vibration only locally occurs in a molecule rather than the collective motion of molecules. For instance, the mode locating at 1086 cm^{-1} is the symmetric stretching of the C-O bonds in a CO_3 group, yet, the neighboring CO_3 groups do not necessarily follow this motion, and thus, this vibrational mode is categorized as the internal mode. Briefly speaking, the vibrational frequency of the chemical bonds is like a pendulum. The shorter the chemical bond is, the higher frequency is; similarly, the heavier the atom is, the lower the frequency is.

In our Raman system, we used a Coherent (brand) continuous wave (constant amplitude and frequency) 532 nm Sapphire (brand) diode laser to irradiate the sample through Olympus (brand) optical microscope with a 20× objective. The scattered Raman signal was typically detected and analyzed by the Horbia Jobin Yvon (brand) spectrometer for 1-10 seconds depending on the intensity of signals. The resolution of the spectrum is around 2 cm^{-1} .

2.2.2. Spin state characterization by Raman spectroscopy

Our study mainly focused on the vibrational mode termed ν_1 at around 1086 cm^{-1} due to its strongest intensity. This is because other peaks become weak after compression [27]. Farfan et al. [27] reported that a low spin ν_1 peak appears when the spin transition occurs, while the high spin ν_1 peak almost disappears as the spin

transition completes. Lin et al. 2012 [6] reported more details that the high spin ν_1 peak becomes a weak satellite peak, rather than totally disappears after the spin transition completes. Indeed we also found this weak satellite ν_1 peak after spin transition completes, supporting Lin's observation.

Such evolution of the Raman spectra across the spin transition enables us to characterize the extent of low spin state by using the relative areas of the ν_1 mode for high and low spin states (**Fig. 7**). Firstly, we subtracted the background of the spectrum and defined the area below the high spin ν_1 mode and low spin ν_1 mode as $A_{\nu_1}^{HS}$ and $A_{\nu_1}^{LS}$, respectively. Secondly, we used the software, PeakFit (<https://systatsoftware.com/products/PeakFit/>), to calculate the ratio of the area of low spin ν_1 mode ($A_{\nu_1}^{LS}$) to the sum of the area of low and high spin ν_1 modes ($A_{\nu_1}^{LS} + A_{\nu_1}^{HS}$) in the Raman spectrum of mixed-spin state siderite. Thirdly, it is improper to express the contribution of satellite peak as " $A_{\nu_1}^{HS}$ " when the spin transition completes since there should be no high spin iron left after spin transition completes. Thus the term $A_{\nu_1}^{HS}$ is rewritten as $A_{\nu_1}^{Satellite}$ after the spin transition completes at the pressure greater than 55 GPa, and we calculated the ratio of the area of low spin ν_1 mode ($A_{\nu_1}^{LS}$) to the sum of the area of low spin ν_1 mode and satellite ν_1 modes ($A_{\nu_1}^{LS} + A_{\nu_1}^{Satellite}$) in the Raman spectrum after spin transition completes at around 65 GPa. The value of $A_{\nu_1}^{LS} / (A_{\nu_1}^{LS} + A_{\nu_1}^{Satellite})$ is typically around 88%. Finally, we divided the

$A_{v_1}^{LS} / (A_{v_1}^{LS} + A_{v_1}^{HS})$ by $A_{v_1}^{LS} / (A_{v_1}^{LS} + A_{v_1}^{Satellite})$ to normalize the proportion of areas

into the degree which is certainly contributed by the low spin iron. The

$\frac{A_{v_1}^{LS} / (A_{v_1}^{LS} + A_{v_1}^{HS})}{A_{v_1}^{LS} / (A_{v_1}^{LS} + A_{v_1}^{Satellite})}$ is defined as “**Normalized** $A_{v_1}^{LS} / (A_{v_1}^{LS} + A_{v_1}^{HS})$ ”, which is

associated with the fraction of low spin iron and allows us to evaluate the extent of

spin transition at 40-55 GPa.

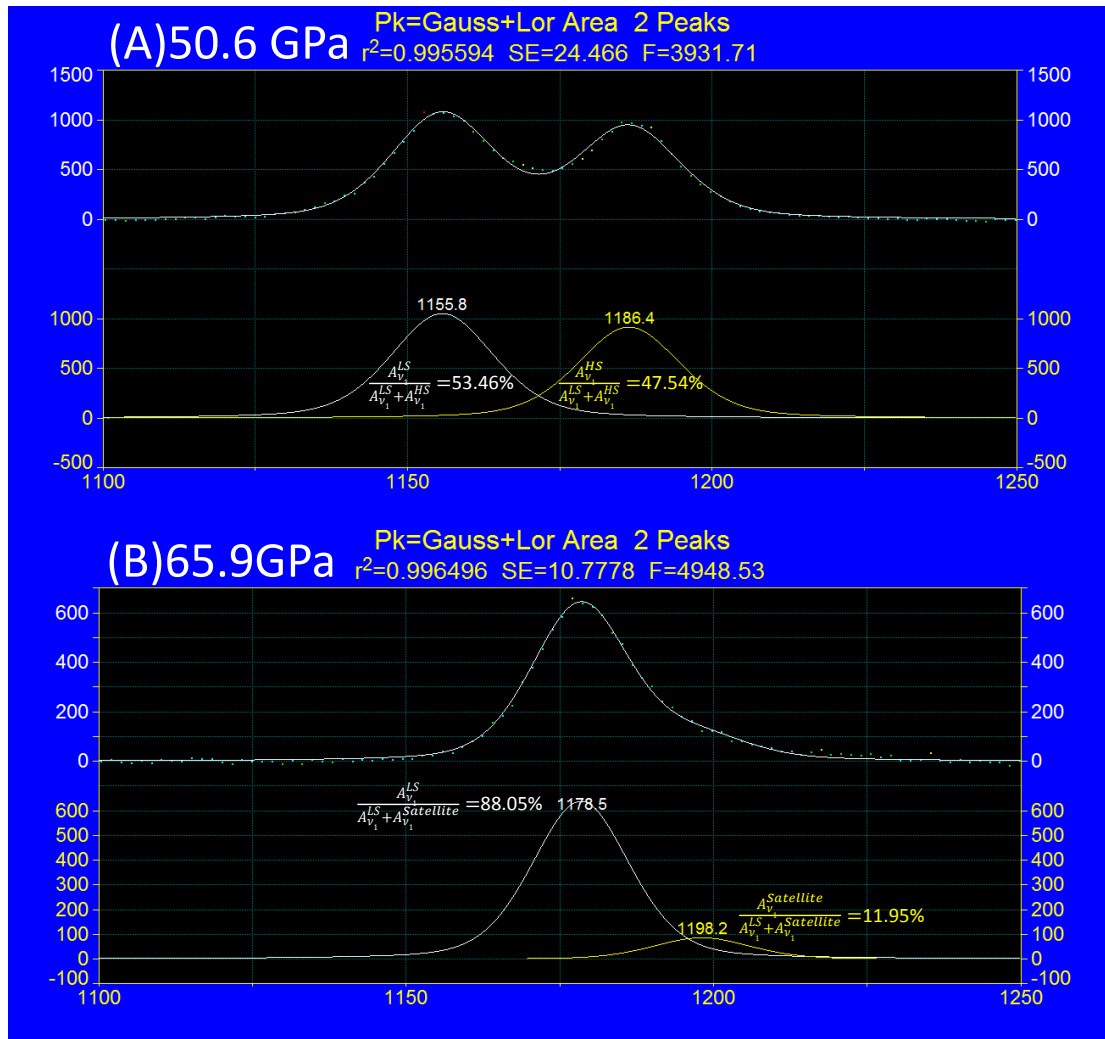


Figure 7. Characterization of fraction of low spin iron by Raman spectrum. Raman spectrum of the ν_1 peak of siderite under 50.6 GPa (A) and 65.9 GPa (B) were fitted by the PeakFit. Both graphs A and B contain two ν_1 peaks. In the graph A, the siderite is under the mixed spin state at 50.6 GPa and the proportion of the relative area of low spin ν_1 mode, $A_{v_1}^{LS} / (A_{v_1}^{LS} + A_{v_1}^{HS})$, is 53.46%. In the graph B, the spin transition has completed at 65.9 GPa and the proportion of the relative area of low spin ν_1 mode, $A_{v_1}^{LS} / (A_{v_1}^{LS} + A_{v_1}^{Satellite})$ is around 88.05%. We divided $A_{v_1}^{LS} / (A_{v_1}^{LS} + A_{v_1}^{HS})$ by $A_{v_1}^{LS} / (A_{v_1}^{LS} + A_{v_1}^{Satellite})$ to normalize the proportion of areas contributed by the low spin iron. Therefore, in this example, the “Normalized $A_{v_1}^{LS} / (A_{v_1}^{LS} + A_{v_1}^{HS})$ ” at 50.6 GPa is $53.46/88.05=60.72\%$.

2.2.3. Comparison of experimental methods characterizing the spin state of siderite

We compare several experimental methods used to characterize the fraction of the spin state of siderite as shown in **Table 2**. Some of the literature only use their experimental method as a standard to determine the onset of spin transition and some of them tried to give a precise extent of the spin state. As shown in the **Table 2**, an advantage of Raman spectroscopy is that it can probe the spin state of iron in siderite or iron-bearing carbonates within a relatively short time (several seconds to several minutes); whereas, some of the conventional methods to probe the spin state of iron in a material, for example, Mössbauer spectroscopy, require several hours to several days to complete the data collection of a pressure point. The second advantage is that the beam size of Raman is relatively small, which means the Raman spectroscopy can provide better spatial resolution, allowing us to distinguish the spin state across the sharp spin state boundary.

However, the pattern of split ν_1 peak in the Raman spectrum results from the softening of C-O bonds vibration during the spin transition and the softening of C-O bonds vibration is a secondary phenomenon. Moreover, there is no literature confirming that the precise fraction of low spin iron can be determined by the Raman spectroscopy. The Raman spectroscopy in this study might not provide the precise

fraction of low spin state, and therefore, in this study, we are not going to claim that we determine the precise fraction of low spin state; instead, we use “**Normalized** $A_{\nu_1}^{LS} / (A_{\nu_1}^{LS} + A_{\nu_1}^{HS})$ ” to describe the extent of spin transition. However, even the Raman spectroscopy cannot probe the precise fraction of low spin iron, the short collection time and great spatial resolution of Raman spectroscopy allow us to simply characterize the extent of spin transition to a certain degree of accuracy within relatively short time.

Comparison of experimental methods characterizing the spin state of iron in siderite

Literatures	This study	Cetantola et al. [28]	Weis et al. [29]	Mattila et al. [30]	Lin et al. [6]
Experimental method	Raman spectroscopy	Mössbauer spectroscopy	X-ray Raman scattering	X-ray emission spectroscopy	X-ray diffraction
Typical collection time	1-10 seconds per pressure point	2-4 days per pressure point	4-12 hours	*Empirically 30 minutes-6 hours per pressure point	*Empirically several seconds
Sample size	45-90 μm ×45-90 μm single crystal	15-20 μm single crystal	15 μm ×15 μm ×25 μm single crystal	Average 5 μm grain size powder	18 μm -thick, 45-50 μm -radius powder disk
Spot size	2-5 μm ×2-5 μm	10 μm ×15 μm	10 μm ×20 μm	120 μm ×55 μm	5-10 μm ×5-10 μm
Utilize synchrotron radiation	No	Yes	Yes	Yes	Yes
Show the fraction of low spin state in the literature	Testing, not confirmed by any study	No	Yes	No	Yes

*Empirical collection time. Collection time information was not mentioned in the literature.

Table 2. Comparison of several experimental methods used to characterize the spin state of iron in siderite. According to the row of collection time, the collection time of Raman spectroscopy is shorter than most of the methods. In the row of spot size, the beam size of Raman spectroscopy is smaller than most of the methods, which means the Raman spectroscopy can provide better spatial resolution to study spin state across sharp spin transition front.

2.3. High-pressure experimental setup

We used diamond anvil cell (DAC) to generate high-pressure conditions in this study (**Fig. 8**).

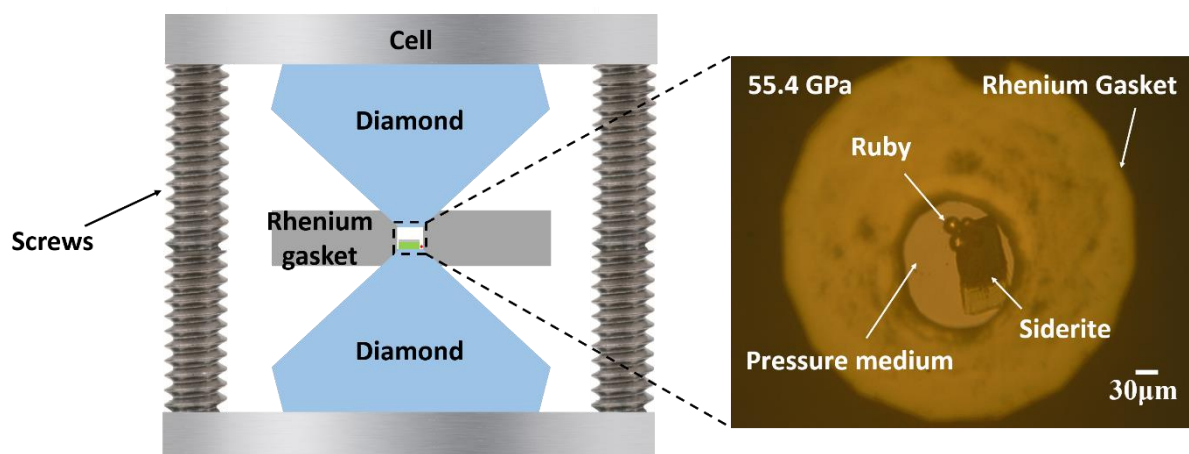


Figure 8. Setup of diamond anvil cell. There are four screws on the cell allowing us to compress the sample by turning the screws. The silicone oil, ruby, and sample are loaded into the sample chamber.

Firstly, we used a pair of diamonds with 300 μm -diameter culets because the area of 300 μm -diameter culets is tiny enough to generate pressure up to 90 GPa. We used the Re gasket due to its great stiffness. The Re gasket was pre-indented to 25 GPa. The thickness of gasket under 25 GPa is around 30-35 μm , allowing us to load 25 μm -thick sample; the gasket was drilled with a 120 μm -diameter hole as the sample chamber after it was pre-indented to 25 GPa.

Secondly, the sample and ruby balls were loaded into the sample chamber. The ruby balls were used to calibrate the pressure by their fluorescence. This method was firstly proposed by Barnett et al. [31] and further developed by Mao et al. [32].

The most conventional equations used to calculate the pressure by Ruby's fluorescence in current high-pressure studies are shown below, where λ_0 is the wavelength of R_1 fluorescence peak of ruby under ambient condition and λ is the wavelength of R_1 fluorescence peak under high pressure.

$$\text{Non-hydrostatic state: } P (\text{Mbar}) = 3.808 [(\lambda/\lambda_0)^5 - 1] \quad (1)$$

$$\text{Hydrostatic state: } P (\text{Mbar}) = 2.484 [(\lambda/\lambda_0)^{7.665} - 1] \quad (2)$$

We used the ruby fluorescent to characterize λ_0 and λ and calculated the pressure within the sample chamber. We used the spectrometer function of our Raman system to characterize the fluorescence of Ruby (note that we did not measure the Raman spectrum of Ruby) and we converted the wavenumber of R_1 fluorescence peak measured by the Raman system into its wavelength to make it can be calculated by the equation (1) and equation (2).

Thirdly, we loaded the silicone oil as a pressure transmitting medium. Due to the low thermal conductivity of silicone oil, the silicone oil can provide better accuracy in the thermal conductivity measurement done by the time-domain thermoreflectance method. This is because if the thermal conductivity of pressure medium is higher, the pressure medium will contribute a higher uncertainty, and thus, decreases the accuracy of measurement. For instance, if the thermal conductivity of two pressure media, A and B, are $1 \text{ W m}^{-1} \text{ K}^{-1}$ and $50 \text{ W m}^{-1} \text{ K}^{-1}$, respectively, and

both estimated ratio of uncertainty of the thermal conductivity of A and B under high pressure are 10 %, then the value of uncertainty propagated by A is $0.1 \text{ W m}^{-1} \text{ K}^{-1}$, whereas, the value of uncertainty propagated B is $5 \text{ W m}^{-1} \text{ K}^{-1}$. The B will propagate a greater uncertainty, causing a greater error in the measurement. Therefore, we chose the silicone oil as a pressure medium to improve the accuracy of high-pressure thermal conductivity measurement. However, according to Klotz et al. [33], the silicone oil could not maintain hydrostatic state after 12 GPa, which might contribute some error to the pressure calibration, yet, we still used the hydrostatic state formula to approximate the pressure in the sample chamber. Indeed, there is no obvious difference between equation (1) and equation (2) until 85 GPa, which is beyond the pressure range we studied. Therefore, although the silicone oil cannot maintain hydrostatic state under high pressure, it is still a reasonable choice in this study. The calculated results of two formulas are shown below (**Fig. 9**).

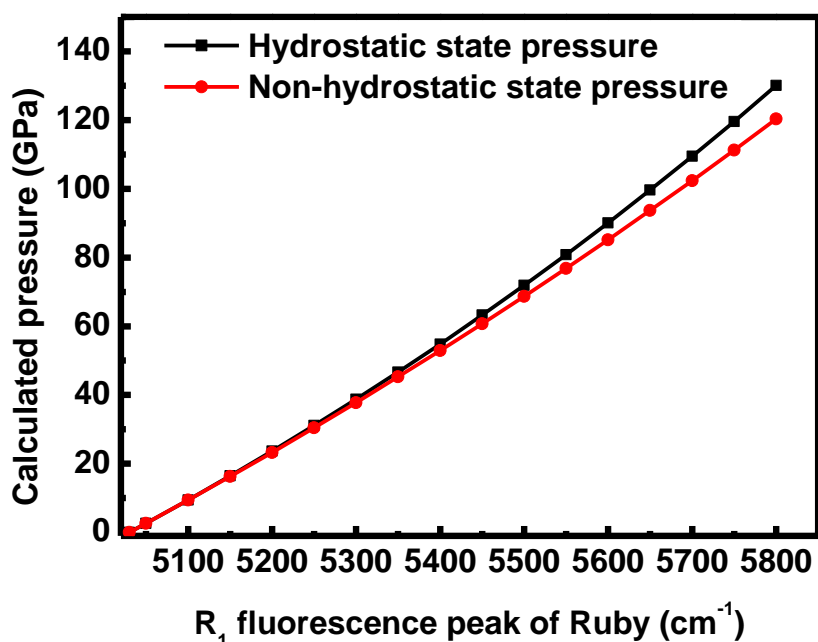


Figure 9. Pressure derived from hydrostatic and non-hydrostatic equations. Black line and red line are pressures derived from hydrostatic formula and non-hydrostatic formula using Eq. 1 and Eq. 2, respectively. The differences between the values of pressure derived from these two formulas are insignificant within the pressure range in this study (0-70 GPa).

2.4. Time-domain thermoreflectance (TDTR)

TDTR is an ultrafast optical pump-probe method to measure the thermal conductivity. The setup of TDTR is shown in the schematic drawing below (**Fig. 10**). In the TDTR measurements, the output of a mode-locked Ti: sapphire laser with 785 nm wavelength was split into a pump beam and a probe beam, which were used to heat the aluminum film coated on the sample and measure the temperature variation of the aluminum film coated on the sample, respectively. The reflectivity of Al film varies slightly as the temperature of Al film changes. This phenomenon is termed thermoreflectance. The pump beam heated the Al film on siderite sample to create a

local temperature variation and the probe beam subsequently measured the reflectivity changes via temperature variation of the Al film. The intensity variation of the reflected probe beam represented the temperature change of the Al film, and it was recorded as voltage changing with delay time by a lock-in amplifier.

The thermal conductivity of the sample controls the cooling rate of Al film, which is associated with the reflectivity change and hence changes the voltage-time variation recorded in the lock-in amplifier. The voltage variation was recorded by the lock-in amplifier as form: $V(t) = V_{in}(t) + iV_{out}(t)$. The in-phase V_{in} and out-of-phase V_{out} components is related to the variation of the reflected probe beam intensity. We analyzed the ratio, $-V_{in}/V_{out}$, as a function of delay time and calculated the thermal conductivity in our thermal model. The graphs of ratio, $-V_{in}/V_{out}$, as a function of delay time were fitted by our model to derive the proper thermal conductivity. The more details of the time-domain thermorefectance method can be found in Hsieh [20].

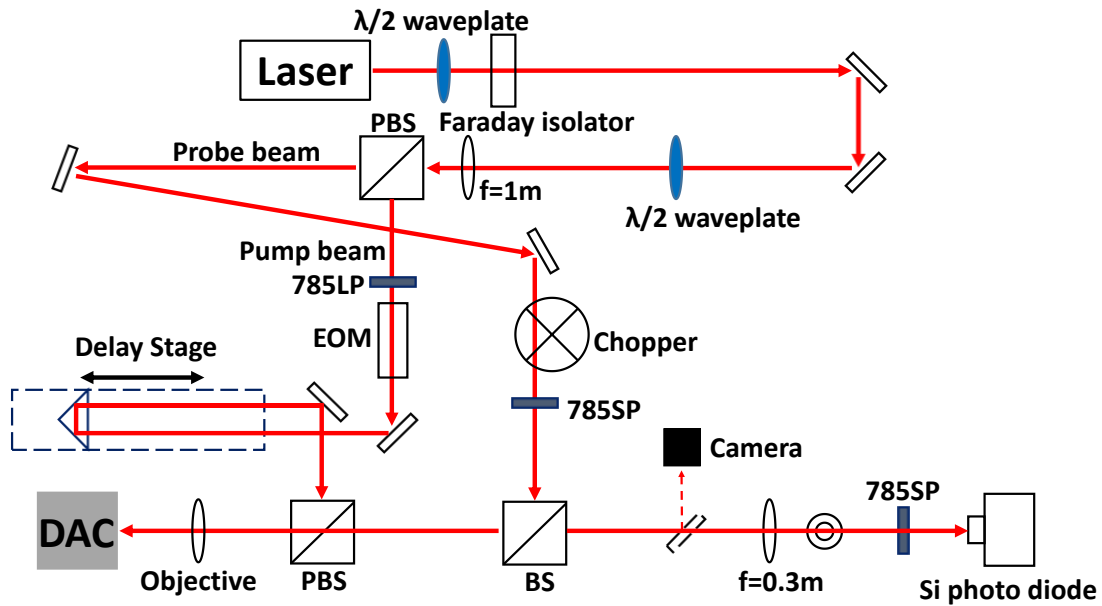


Figure 10. Setup of TDTR. A linearly polarized laser is emitted from a mode-locked Ti: sapphire laser source. The first $\lambda/2$ waveplate is used to adjust the power of laser that can penetrate it by changing the angle of the grating, which is the relevant power used in the measurement. The Faraday isolator is used to block the reflected beam to return to the source, preventing the source from being damaged. The second $\lambda/2$ waveplate is used to adjust the polarized plane of light and, thus it can be divided by the first polarized beam splitter (PBS) into any ratio of pump power to probe power; The ratio of pump power to probe power is typically 2:1. The pump beam will go through the 785 long pass filter (785 LP), which is a filter allowing the light with the wavelength longer than 785 nm to penetrate. The EOM is an electro-optical modulator shuttering in the frequency of 8.7 MHz, making the pump beam irradiate the sample 8700000 times per second. The delay stage is a mobile retroreflector controlling path length of pump beam to generate arrival time difference between the pump beam and probe beam. The probe beam is chopped by the 200 Hz chopper for double modulation [34]. Then the probe beam goes through the short pass filter (785 SP), a filter allowing the light with the wavelength shorter than 785 nm to penetrate, after the chopper; this is because we have to separate the frequencies of pump and probe beams to prevent the scattered or stray pump beam from interfering our signals. Then the pump and probe beams reach the polarized beam splitter (PBS) and beam splitter (BS), respectively, these two devices reflect the light to the sample but prevent the reflected light from returning to their original paths. The 785 SP in front of the Si photodiode is used to prevent the pump beam from reaching the photodiode. The probe beam is reflected by the aluminum film to the Si photodiode. The signal was then further enhanced by a preamplifier and recorded by a radio-frequency lock-in amplifier to convert into in-phase V_{in} and out-of-phase V_{out} signal.

2.5. Thermal model and parameters in the TDTR analysis

2.5.1. Configuration of the thermal model

The thermal model that we used to analyze the data in TDTR measurements contains several parameters. The configuration and parameters are shown in **Fig. 11**.

The thermal model consists of five layers, the silicone oil, the aluminum film, the sample, the silicone oil-Al interface, and Al-siderite interface. The thermal properties of each layer contribute differently to the temperature distribution in the model.

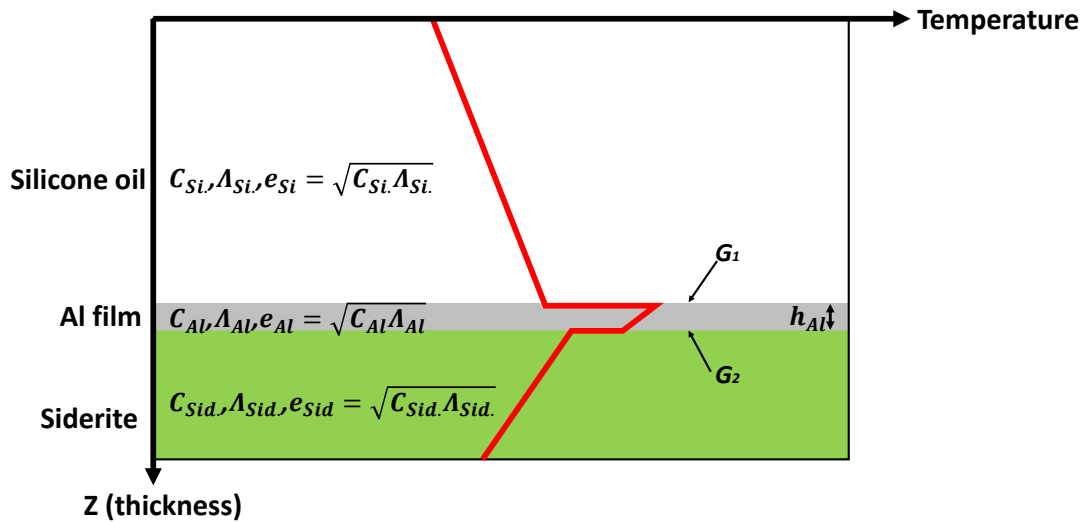


Figure 11. Schematic drawing of thermal model. The red curve is the temperature profile after the aluminum film is heated by laser and the heat diffuses into the silicone oil and siderite sample assuming the laser is incident from the silicone oil side. The h_{Al} is the thickness of the aluminum layer. G_1 and G_2 are the thermal conductance parameters of the interfaces between silicone oil and Al as well as between Al and siderite, where the higher the G is, the lower the temperature drop at the interface is. The Λ is the thermal conductivity of each layer with unit $W m^{-1} K^{-1}$. The C is the volumetric heat capacity of each layer with unit $J cm^{-3} K^{-1}$, and the e is the thermal effusivity defined as $e = \sqrt{\Lambda C}$.

To derive the thermal conductivity, we considered the thermal effusivity of each layer, which is defined as $e = \sqrt{\lambda C}$, where λ is the thermal conductivity of the material and C is the volumetric heat capacity. The thermal effusivity determines the rate of heat transfer between two contacting objects with different temperature. The aluminum film cools down faster while the thermal effusivity of the sample is higher.

2.5.2. Thermal conductivity and heat capacity of the silicone oil layer

The thermal conductivity of silicone oil (λ_{Si}) under high pressure and room temperature was measured by Hsieh [19] with the TDTR technique. Hsieh's study [19] assumed that the volumetric heat capacity of silicone oil is a constant of $1.4 \text{ J cm}^{-3} \text{ K}^{-1}$ due to the absence of a reliable method to derive the heat capacity of silicone oil at high pressures. We used Hsieh's data to estimate the thermal conductivity variation of silicone oil under high-pressure condition by fitting Hsieh's data with a polynomial. The equation is shown below, where P is the pressure with a unit GPa.

$$\lambda_{Si} (\text{W m}^{-1} \text{K}^{-1}) = 0.18 + 0.12 P - 5.58 \times 10^{-3} P^2 + 1.78 \times 10^{-4} P^3 - 3.21 \times 10^{-6} P^4 + 3.20 \times 10^{-8} P^5 - 1.64 \times 10^{-10} P^6 + 3.39 \times 10^{-13} P^7 \quad (3)$$

The volumetric heat capacity of silicone oil in this study is also assumed to be a constant of $1.4 \text{ J cm}^{-3} \text{ K}^{-1}$ as Hsieh's study [19]. The uncertainty of this assumption

will be discussed in **section 3.4**.

2.5.3. Thermal conductivity and heat capacity of the aluminum layer

The thermal conductivity of aluminum is $200 \text{ W m}^{-1} \text{ K}^{-1}$ measured by Hsieh et al. [20], and it is assumed to be a constant in this study because the thermal conductivity variation of aluminum under high pressure still requires further investigations. However, the error contributed by the thermal conductivity of aluminum is minor. This is because the thermal model is not sensitive to the thermal conductivity of aluminum. We will show the minority of error caused by the uncertainty of thermal conductivity of aluminum in **section 3.4**.

The heat capacity of aluminum significantly affects the derived value of thermal conductivity, and thus, it influences the accuracy of our conclusions. We cannot assume the heat capacity of aluminum to be a fixed value. The heat capacity of aluminum was estimated by Hsieh et al. [20] with Debye temperature variation of aluminum [35]. The heat capacity of most of the materials above Debye temperature is almost a constant, $C_v=3R$, which is also known as Dulong-Petit law, where the C_v is the molar heat capacity at constant volume and R is the ideal gas constant. Below the Debye temperature, the heat capacity of material decreases as its temperature

decreases. However, the high-pressure will change the volume, density and elastic properties of a material. Therefore, under high pressure, the difference between the current temperature of the material and its Debye temperature could be different from the ambient condition, influencing the accuracy of heat capacity. The formula estimating volumetric heat capacity of aluminum under high pressure is shown below, where the unit of P is GPa.

$$C_{Al} (J cm^{-3} K^{-1}) = 2.44 + 1.63 \times 10^{-2} P - 4.47 \times 10^{-4} P^2 + 5.99 \times 10^{-6} P^3 - 3.23 \times 10^{-8} P^4 \quad (4)$$

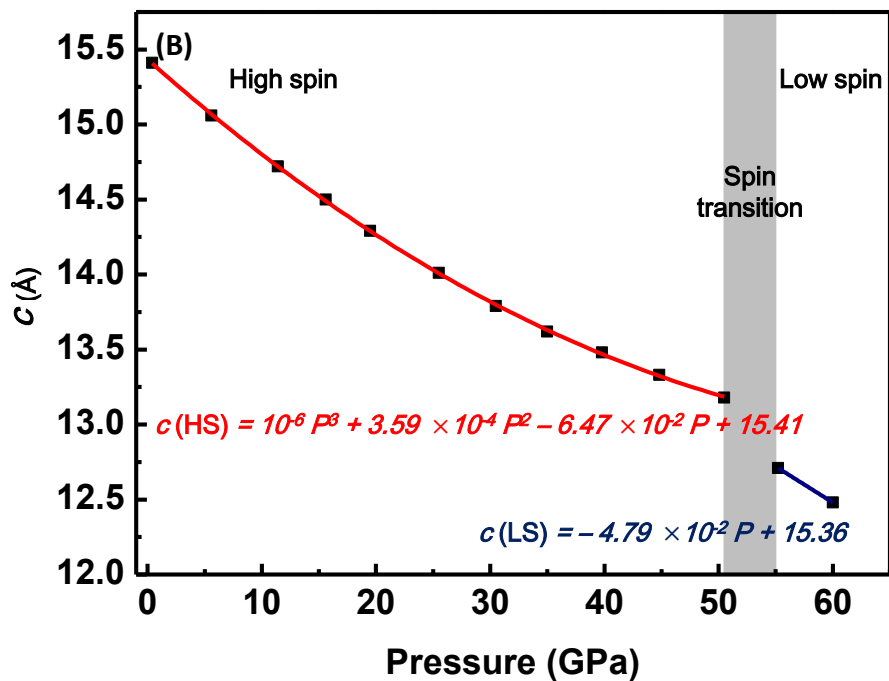
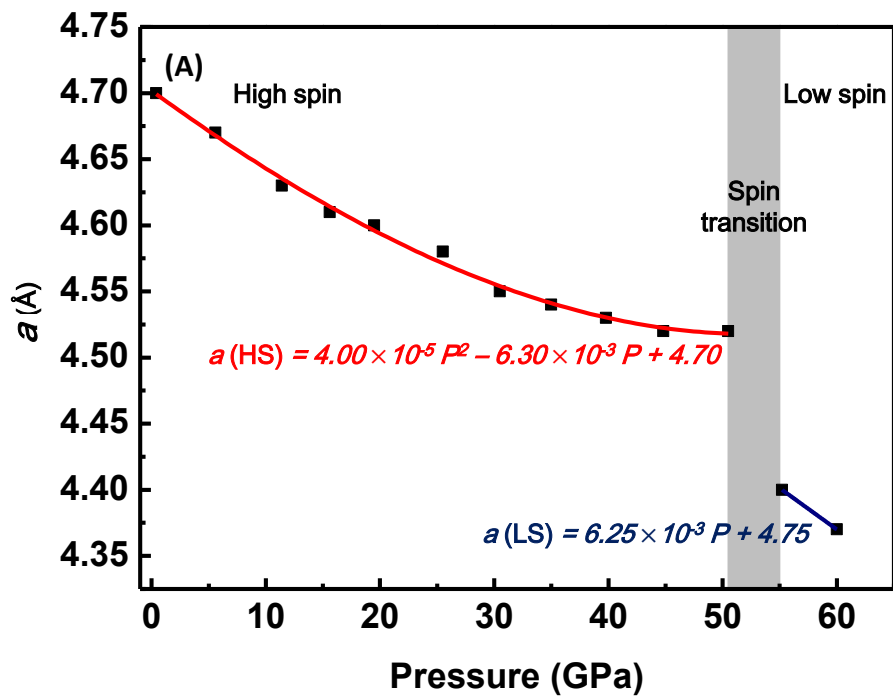
2.5.4. Thickness of aluminum layer

It is difficult to measure the thickness of aluminum under high pressure directly. This is because the acoustic signal of aluminum under high pressure may not be clear enough to allow us to calculate the thickness of aluminum. We instead utilized the volume change of siderite to help us estimate the thickness of aluminum under high pressure indirectly. Some studies have interpreted the details of the changes in unit cell volume and/or lattice parameters of siderite under high pressure, for example, Litasov et al. and Farfan et al. [9, 27]. We utilized the results done by Farfan et al. [27] because this study contains XRD data and lattice parameters of siderite up to 60 GPa, whereas Litasov et al. [9] only studied the parameters variations

up to 33GPa. We plot the equation of state of siderite across the spin transition of iron in **Table 3** and **Fig. 12**. The composition of ($\text{Fe}_{0.76}\text{Mn}_{0.15}\text{Mg}_{0.09}\text{Ca}_{0.01}\text{CO}_3$) siderite in Farfan et al. [26] is sufficiently close to the siderite composition in this study, ($\text{Fe}_{0.78}\text{Mg}_{0.22}\text{CO}_3$). Although the Mn^{2+} ion in Farfan's study might also undergo the pressure-induced spin transition, no evidence shows Mn^{2+} undergoes spin transition below 54 GPa and the precise pressure that the Mn^{2+} undergoes spin transition may be much higher [36]. This is because of the smaller crystal field splitting energy for Mn^{2+} and the radius of Mn^{2+} in MnCO_3 . The radius of Mn^{2+} (0.83 nm) is larger than Fe^{2+} (0.78 nm), and thus it increases the Mn-O bond length and higher pressure is required to compress Mn and O to be close enough to undergo the spin transition. Since the Mn^{2+} does not interfere Farfan's observation [26], the XRD results in Farfan et al. [26] is sufficiently justified to provide a pertinent reference in this study.

<i>P</i> (GPa)	<i>a</i>(=<i>b</i>) (Å)	<i>c</i> (Å)	<i>V</i> (Å³)
0.4	4.70	15.41	295.28
5.6	4.67	15.06	282.75
11.4	4.63	14.72	273.61
15.6	4.61	14.50	266.80
19.5	4.60	14.29	261.20
25.5	4.58	14.01	254.10
30.5	4.55	13.79	247.60
35.0	4.54	13.62	243.50
39.8	4.53	13.48	239.60
44.8	4.52	13.33	235.90
50.5	4.52	13.18	232.60
55.2	4.40	12.71	213.40
60.0	4.37	12.48	206.80

Table 3. Lattice parameters and volume of the unit cell of siderite from 0.4 to 60 GPa. The data were cited from Farfan et al. [26].



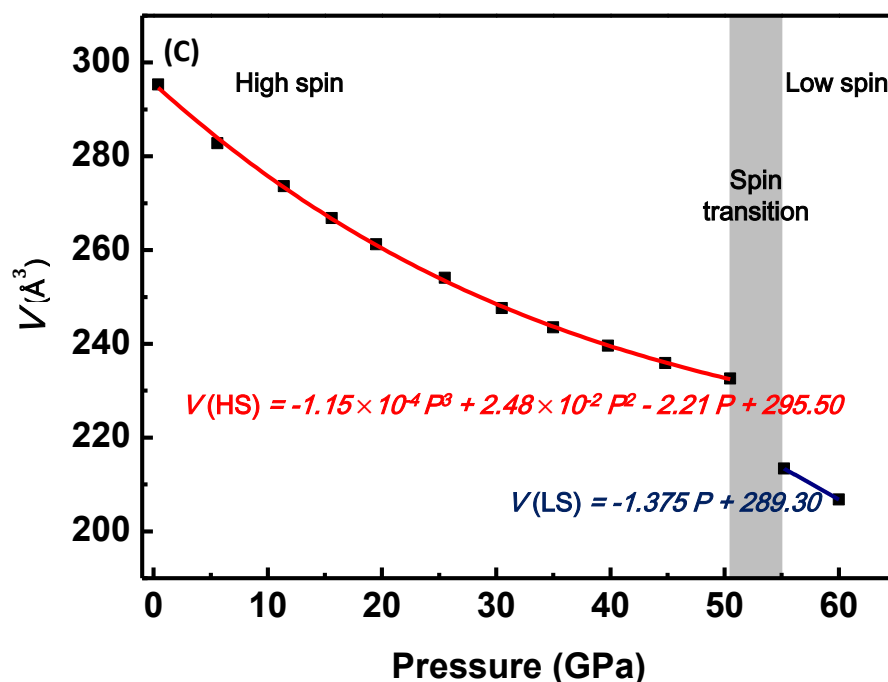


Figure 12. Lattice parameters of siderite as a function of pressure. (A) The lattice parameter a as a function of pressure. The diagram shows that the length of unit cell along the a -axis decreases smoothly until 50.5 GPa and drastically drops upon the onset of the spin transition. (B) The lattice parameter c as a function of pressure. The diagram shows a similar tendency as the lattice parameter a . (C) The volume of the unit cell as a function of pressure shows that the volume of the unit cell decreases around by 20 \AA^3 (10%) upon the onset of spin transition.

By utilizing these data, we built the equation of state of siderite under high pressure to predict the volume change and area change of sample. Note that graphs A and B in **Fig. 12** show that the lattice parameters do not decrease smoothly from 0.4 to 60 GPa because there is a sudden drop once the spin transition occurs, and thus we must build two equations of state at different spin states. We fit the data before 50.5 GPa by a third-order polynomial to represent the equation of state before the spin transition. However, the equation of state after spin transition could only be estimated

from two data points after the spin transition (55.2 GPa and 60.0 GPa). According to graphs A, B, and C in **Fig. 12**, the lattice parameters vary almost linearly within the range of 20 GPa section when the pressure is below 50 GPa (e.g. 0-20 GPa, 10-30 GPa, etc.). Thus the remnant pressure range after the spin transition (50-70 GPa) is proper to assumed to be almost a linear function. The function of the variation of a and c as a function of pressures are shown below, where P is the pressure in GPa. The lattice constants of the a -axis and c -axis of siderite under ambient condition are 4.70 Å and 15.41 Å, respectively.

Lattice constants of a ($= b$) before spin transition:

$$a (\text{Å}) = 4.00 \times 10^{-5} P^2 - 6.30 \times 10^{-3} P + 4.70 \quad (5)$$

Lattice constants of a ($= b$) after spin transition:

$$a (\text{Å}) = 6.25 \times 10^{-3} P + 4.75 \quad (6)$$

Lattice constants of c before spin transition:

$$c (\text{Å}) = 10^{-6} P^3 + 3.59 \times 10^{-4} P^2 - 6.47 \times 10^{-2} P + 15.41 \quad (7)$$

Lattice constants of c after spin transition:

$$c (\text{Å}) = -4.79 \times 10^{-2} P + 15.36 \quad (8)$$

We also needed the volume variation of aluminum under high pressure to calculate the thickness change of aluminum film under high pressure. Therefore, we utilized the equation of state of aluminum from Bercegeay and Bernard [37]. The

equations of state of aluminum and siderite are shown below, where P is the pressure in GPa.

Density variation of aluminum under high pressure:

$$\rho_{Al} (kg\ m^{-3}) = 2700 [(P + 17.77)/17.77]^{0.2222} \quad (9)$$

We already knew the thickness of aluminum under ambient condition. We assumed that the edge of the aluminum layer was fixed on the edge of the sample. By combining the equations (5-8) with equation (9), we calculated the thickness variation of the aluminum layer by calculating the area variation of the sample. For example, assuming that there is an aluminum film coated on a siderite sample with a -axis upward and its initial thickness at ambient pressure is 80 nm, as the pressure raises to 10 GPa, the density of aluminum becomes 2981.58 kg m⁻³, which means the volume of aluminum decreases by 9.44%, and the lattice constants of siderite along the a -axis and c -axis decrease by 1.25% and 3.96%, respectively. Hence, we estimated the thickness decrease of the aluminum layer coated on a -axis siderite under 10 GPa is 9.44-1.25-3.96=4.2%. In other words, an aluminum with 80 nm-thick initial thickness coated on an a -axis upward sample becomes 76.64 nm-thick when pressure raise to 10 GPa.

2.5.5. Heat capacity of siderite

The heat capacity of the sample is essential to derive the thermal conductivity of the sample in our model because it is one of the parameters that contribute to the thermal effusivity of sample layer. However, in this study, we were restricted by the unavailability to measure the heat capacity of the sample in DAC. Hence, we could only assume that the heat capacity of siderite is a constant under pressure, but this is a reasonable assumption. The number of atoms per unit volume increases while siderite is compressed because the density of siderite increases and each atom in the unit volume carries some heat capacity. If the number of atoms per unit volume increases, the volumetric heat capacity of siderite is expected to increase with pressure, yet, compression also increases the Debye temperature of materials. The increasing Debye temperature decreases the amount of heat capacity that every atom carries. These two effects cancel each other and make the volumetric heat capacity of material vary slightly as pressure raises. The volumetric heat capacity of siderite under room pressure and room temperature is $2.83 \text{ J cm}^{-3} \text{ K}^{-1}$ calculated from molar heat capacity of siderite [38], the formula weight and density of siderite: $82.69 \text{ (J mol}^{-1} \text{ K}^{-1}) / 115.86 \text{ (g mol}^{-1}) \times 3.96 \text{ (g cm}^{-3}) \approx 2.83 \text{ (J cm}^{-3} \text{ K}^{-1})$.

2.5.6. Thermal conductance of interfaces

Interface thermal conductances (G_1 and G_2) are two unknown parameters in our thermal model. G_1 is the interface thermal conductance between the silicone oil and the aluminum film, and G_2 is the interface thermal conductance between the aluminum and the siderite. They contribute to the efficiency of the heat flow across the interfaces. The higher the thermal conductance is, the lower the temperature drop at the interface is.

Thermal conductance typically increases while the pressure raises because the interface bonding stiffness increases, making heat transfer across the interface more efficiently. The G_1 and G_2 were determined by trial and error method in the process of data fitting. We typically assume that the G_1 equals to G_2 even they represented the different interface. The uncertainty of this assumption will be described in **section 3.4**.

2.5.7. Deriving thermal conductivity of sample

After all of the parameters were determined, we derived the thermal conductivity by comparing the measured ratio in TDTR data within the delay time of 90-4000 ps and the ration calculated by the thermal model. The more mathematical calculation details of the thermal model can be found in Cahill [39]. **Fig. 13** shows a representative data for the ratio ($-V_{in}/V_{out}$) of an aluminum film coated on siderite at

1.39 GPa as a function of delay time. Generally speaking, the ratio is basically proportional to $(\sqrt{\lambda_{Si}C_{Si}} + \sqrt{\lambda_{Sid.}C_{Sid.}})/h_{Al}C_{Al}$ at high modulation frequency. For example, the modulation frequency is 87 MHz in this study. Note that the thermal conductivity of aluminum is not included in this formula, showing that the thermal conductivity of aluminum has a minor effect on the thermal model. The thickness and heat capacity of aluminum play a crucial role here, however.

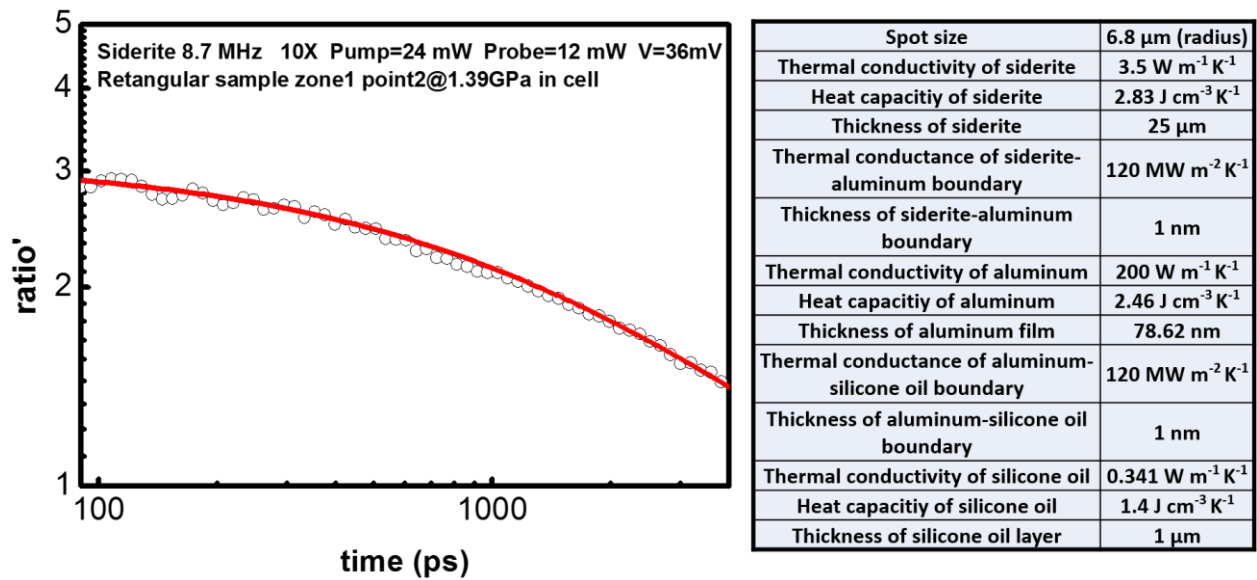


Figure 13. Example data of ratio as a function of delay time under 1.39 GPa. The raw data from the TDTR measurement are shown as open circles in the left-hand graph and the fitting curve derived from the thermal model is shown as the red curve. The parameters in the model that can best fit the raw data are shown in the table on the right-hand side. We used trial and error method to find a combination of known parameters, e.g. heat capacity, and the unknown parameters, such as thermal conductivity of siderite, that could generate a curve best fitting the raw data. By fitting the data, we derive the thermal conductivity of the sample.

CHAPTER 3

RESULTS AND DISCUSSION

3.1. Raman spectra of siderite

We measured the Raman spectra of siderite from 0-67 GPa to study the Raman spectra changes of siderite across spin transition at around 40-55 GPa. The Raman spectrum of siderite under ambient condition contains four noticeable peaks below 1200 cm^{-1} and represent four types of vibrational modes as shown in **Fig. 14**. We also measured the Raman spectrum of pressure medium, silicone oil. In fact, the Raman spectra measured in this study is the combination of siderite data and silicone oil data because the sample and silicone oil were loaded into the DAC together. (**Fig. 14**).

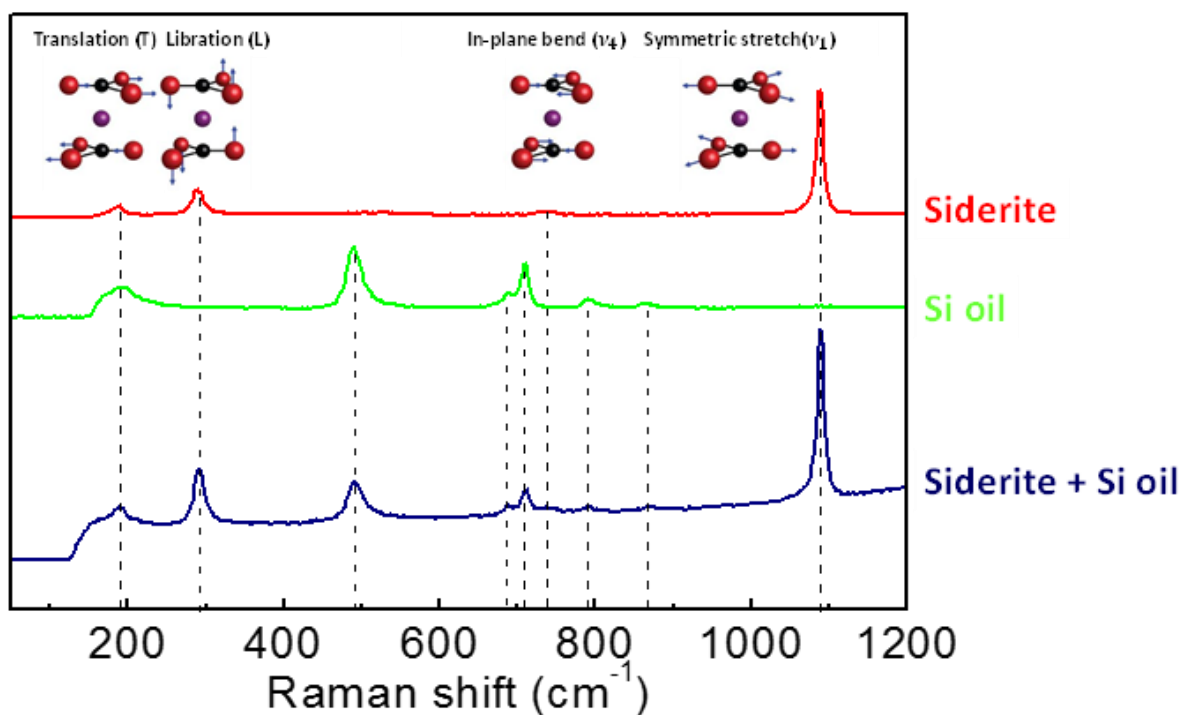


Figure 14. Raman spectra of siderite and silicone oil before compression. The red curve shows the siderite Raman spectrum under ambient pressure and the vibrational modes of the carbonate groups modified from Lin et al. [6] are schematically drawn next to each peak. The green curve is the Raman spectrum of silicone oil, which is the pressure transmitting medium in this study. The blue curve shows the combined spectrum of siderite and silicone oil after the siderite and silicone oil were loaded into the DAC.

In this study, we focused on the peak with the highest intensity in the Raman spectrum of siderite, ν_1 , at around 1086 cm^{-1} , which is a common peak in all of the calcite group minerals resulting from the symmetric stretching mode in the CO_3^{2-} anion [40] and commonly investigated in the carbonate related studies. As shown in **Fig. 15**, our high-pressure Raman spectra indicate that the frequency of ν_1 increases monotonically with pressure until around 49 GPa, in which the length of the C-O bond shrinks, increasing the vibrational frequency. An additional peak with a slightly

lower frequency (wavenumber drops by around 30 cm^{-1}) emerges upon the onset of the spin transition around 49 GPa. This is because during the spin transition, the radius of Fe^{2+} ions shrinks and the volume of Fe-O octahedron collapses upon the spin transition, and consequently, the oxygen is pulled away from the carbon, which lengthens the C-O bonds and softens the vibrational frequency of ν_1 mode [41]. The vibrational frequency of ν_1 softens and jumps back to around 1155 cm^{-1} while the spin transition occurs. Sometimes, we observe two peaks within a very narrow pressure range, showing that the siderite is under mixed-spin state (**Fig. 15**). This is a valid signature of mixed-spin state of siderite.

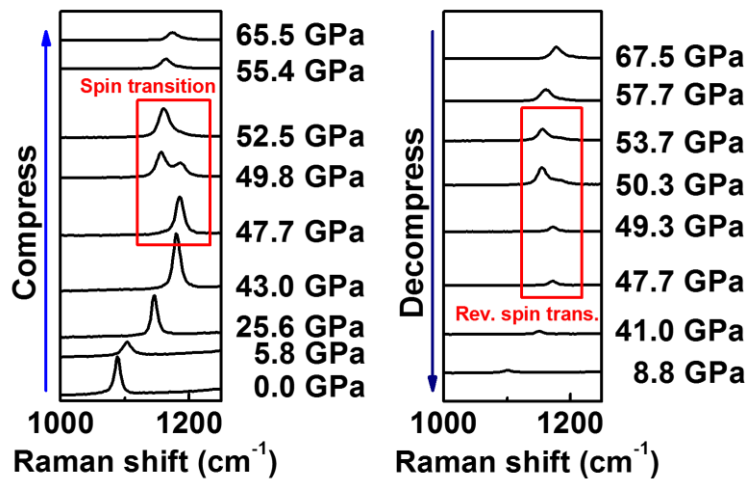


Figure 15. Representative Raman spectra of the siderite during compression and decompression cycles. The frequency of ν_1 symmetric stretching mode in the trigonal carbonate group around 1086 cm^{-1} increases monotonically as pressure raises (left) until around 49 GPa, after which a slightly lower frequency peak appears upon further compression to a mixed spin state. During the decompression, the new peak disappears at 50 GPa (left).

Based on our Raman spectra, we can find that the pressure range of spin transition in this study is consistent with previous studies [6, 7, 27] which used different siderite samples with different iron concentrations. **Fig. 16** compiles the pressure range of the spin transition as a function of iron concentration based on our current study and previous studies [30, 42, 43]. This indicates that the compositional variation of iron in siderite has a minor effect on the pressure range of the spin transition. This result is different from the pressure range of the spin transition for (Mg, Fe)O solid solutions that varies from 40 to 80 GPa, depending on the concentration of iron [44].

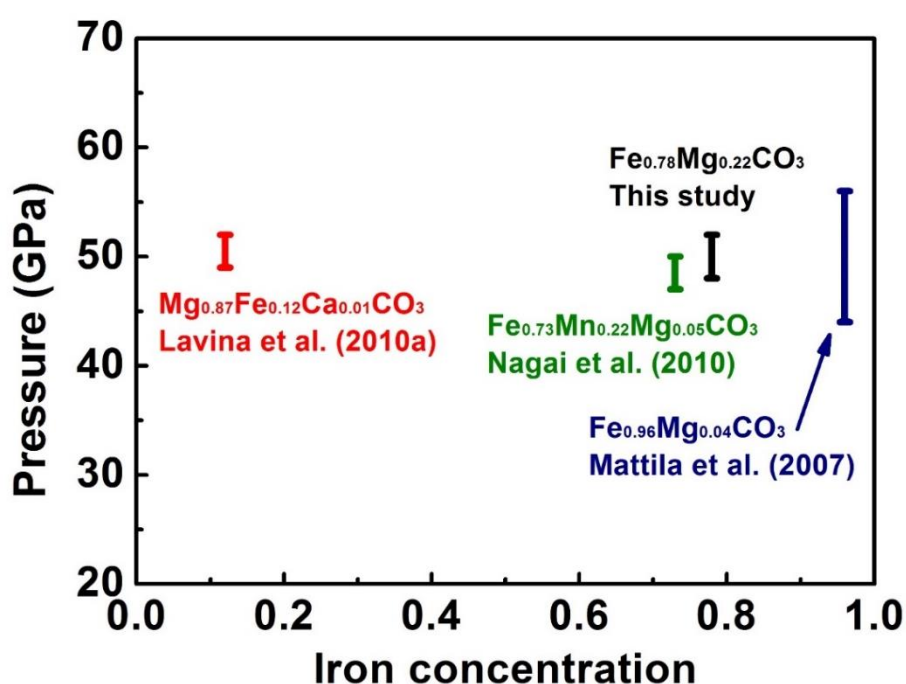


Figure 16. The pressure range of spin transition in several studies. The pressure range of spin transition in siderite is around 40-55 GPa. There is no significant difference among pressure range of spin transition determined by previous studies and this study. Thus we conclude that the iron concentration of iron-bearing carbonates has a minor effect on the onset pressure of spin transition.

The pressure range of spin transition of iron-bearing minerals typically raises with iron concentration. For example, the pressure range of spin transition of (Mg, Fe)O solid solutions raises with the iron concentration [44]. This is because the diameters of metal ions decrease when the spin transition occurs, leading to not only a higher charge density but also a drop of distance among cations. Thus the repulsive force among cations increases and the instability of whole structure declines after spin transition completes. In the low spin state, the higher the density of low spin ions in unit volume, the higher the instability is. To counter the higher repulsive force and stabilize the structure, a higher pressure is required to suppress the repulsive force while the proportion of the ions with spin transition ability arises. As a result, the pressure range of spin transition spin transition, generally speaking, tends to increase with the proportion of the ion with spin transition ability in some minerals. However, the results of siderite seem to contradict this prediction. How could it be possible?

There are two possible explanations that can be used to interpret this phenomenon.

First, the distance between irons within the siderite structure is relatively longer among iron-containing minerals. The arrangement of metal polyhedra in the mineral structure determines the distance between two positive charges (**Fig. 17**). The metal polyhedra in calcite structure share their corners. Thus, in the siderite, the distance between irons is relatively further than other categories of minerals. This

geometric configuration weakens the iron-iron repulsive force while the spin transition occurs (note that the electrostatic force is inversely proportional to the square of distance according to Coulomb's law, and thus, the electrostatic force drops drastically even the distance between irons only slightly increases). Since the repulsive force between irons is relatively weak, it does not require so high pressure to suppress the repulsive force even the amount of iron increases, whereas, the inter-iron distance within (Mg, Fe)O is much shorter (side sharing octahedra), which increases its onset pressure for spin transition with the iron concentration [6].

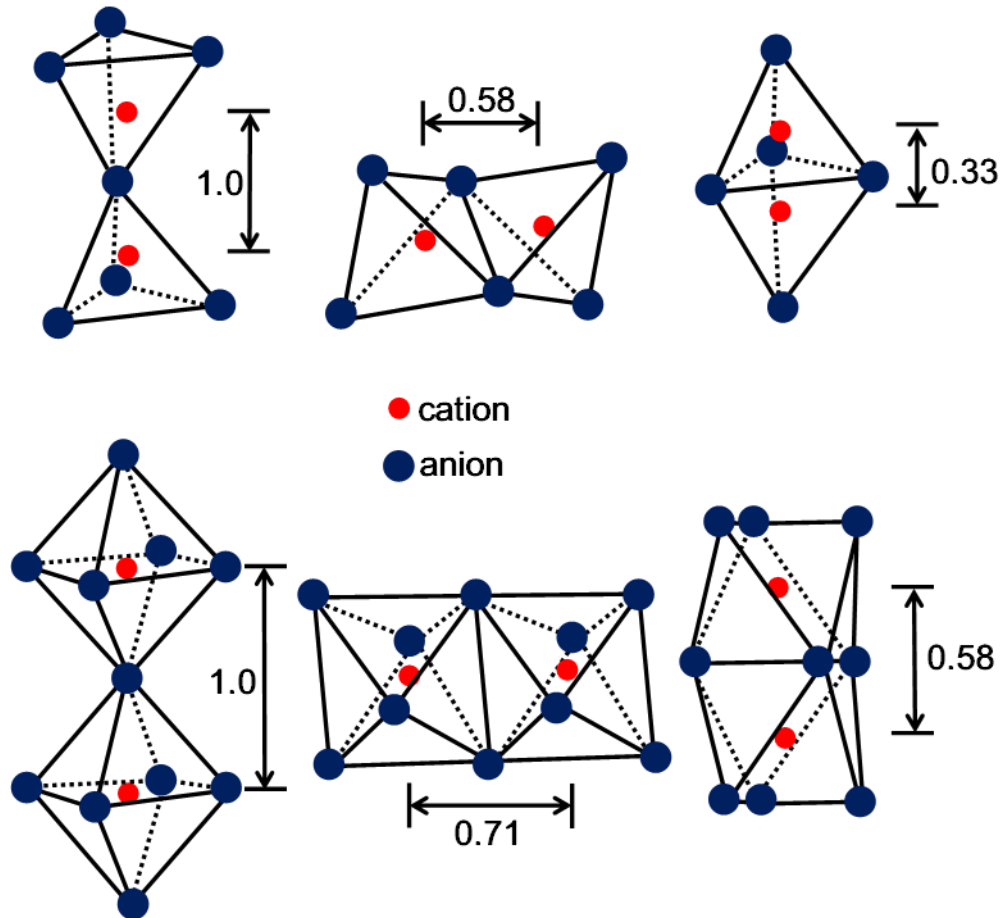


Figure 17. Distance between cations in several forms of metal polyhedra connection arrangements. The initial distance between two neighboring cations sharing the edge of their polyhedrons is assumed to be 1 unit. For tetrahedra, the distance becomes 0.58 unit and 0.33 unit when the tetrahedrons share their edge and face, respectively. For octahedra, the distance becomes 0.71 unit and 0.58 unit when octahedra share their edge and face, respectively. Sharing the corner provides longer distance between two neighboring cations and decreases their repulsive force. In contrast, sharing the edges or faces decreases the distance between two neighboring cations; therefore increases their repulsive. Note that the repulsive increase driven by distance decrease is not linear: the electrostatic force is proportional to $1/r^2$ according to Coulomb's law. Thus, the repulsive force drops substantially even the distance between ions merely slightly increases.

The second possible answer is that because the bulk moduli values do not vary a lot among carbonates [45]. Müller et al. [45] investigated the bulk moduli of several carbonate minerals (e.g., magnesiosiderite, magnesite, rhodochrosite, etc.) measured by former studies [41, 46-48], finding that the differences in elastic properties among

carbonates are minor. Because the CO_3^{2-} is the common component among all of the carbonates, it does not cause any significant variation of elastic constants among carbonates. The differences of elastic constants are expected to be contributed by the elastic properties of metal-oxygen octahedra, which depends on the type of the metal cations. However, the elastic properties of all of the investigated metal-oxygen octahedra are similar. Thus there is no obvious elastic properties difference among carbonates. These discoveries imply that the compressibility of metal-oxygen octahedra, which determines the extent of pressure to make the chemical bonds short enough to generate spin transition, is similar among carbonates. Hence, the concentration of magnesium in the siderite crystal does not change the compressibility of Fe-O bonds, and thus the iron concentration has a minor effect on the pressure range of spin transition of siderite.

3.2. Results of thermal conductivity along *a*-axis

We measured two different locations of an *a*-axis upward sample with TDTR (**Fig. 18**). We plotted the thermal conductivity as a function of pressure and recorded the Raman spectra of siderite to 66 GPa. According to **Fig. 18**, at 0-40 GPa, the thermal conductivity gently increases from $3 \text{ W m}^{-1} \text{ K}^{-1}$ to around $12 \text{ W m}^{-1} \text{ K}^{-1}$ and drastically raises by two times to $35 \text{ W m}^{-1} \text{ K}^{-1}$ at 45-55 GPa accompanied by the spin

transition showed by the Raman spectra of ν_1 mode. Thermal conductivity drops to 7 $\text{W m}^{-1} \text{K}^{-1}$ after 55 GPa, where spin transition completes and gently increases again to 12 $\text{W m}^{-1} \text{K}^{-1}$ at 66 GPa. This result of thermal conductivity variation along a -axis across the pressure range of spin transition implies that the thermal conductivity of siderite may be very sensitive to the spin transition.

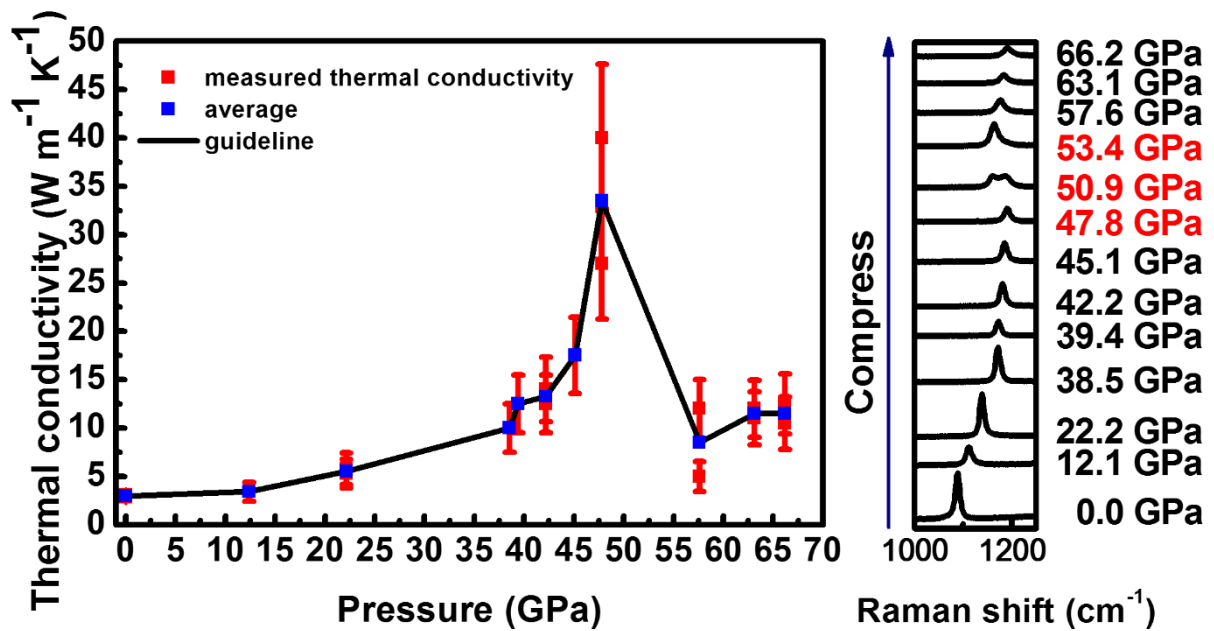


Figure 18. Thermal conductivity of siderite as a function of pressure along a -axis during compression. The red symbols represent the values of thermal conductivity during compression from ambient condition to 66 GPa, the blue symbols are the average of values of thermal conductivity and the black line is a guideline to show the trend of variation. Estimate of the error bars will be discussed in section 3.4. We found that the spin transition in this run occurs slightly before 47.8 GPa and completes at around 53.4 GPa, which agrees well with previous chapter and former studies. The pressure range of spin transition from start to completion in this run is 45-53 GPa and we found that the spin transition may increase the thermal conductivity of siderite. Note that this figure does not include all of the pressure points in the right-hand side Raman spectra. For example, some pressure points, such as 50.9 GPa in the right-hand side Raman spectrum, the V_{in} of TDTR data becomes too weak to be used to analyze the thermal conductivity. This is because the thermorefectance of aluminum diminishes as the pressure ranges are around 6-8 GPa, 25-30 GPa, and 45-55 GPa. The mechanism causing the thermorefectance drop of aluminum can be found in Dandrea and Ashcroft [49].

There is only this set of data of a -axis available in this study. This is because we needed a flat aluminum surface to measure the thermal conductivity by the TDTR, yet, we discovered that some anomaly occurs in siderite after 6 GPa frequently. We suspected that the siderite may form the twin under high pressure, damaging the flatness of aluminum frequently after 6 GPa, or may merely break along its cleavages. Thus, it is very difficult to measure the thermal conductivity along a -axis after 6 GPa. There is a photo showing the damage of aluminum coating layer under 35 GPa as shown below (**Fig. 19**).

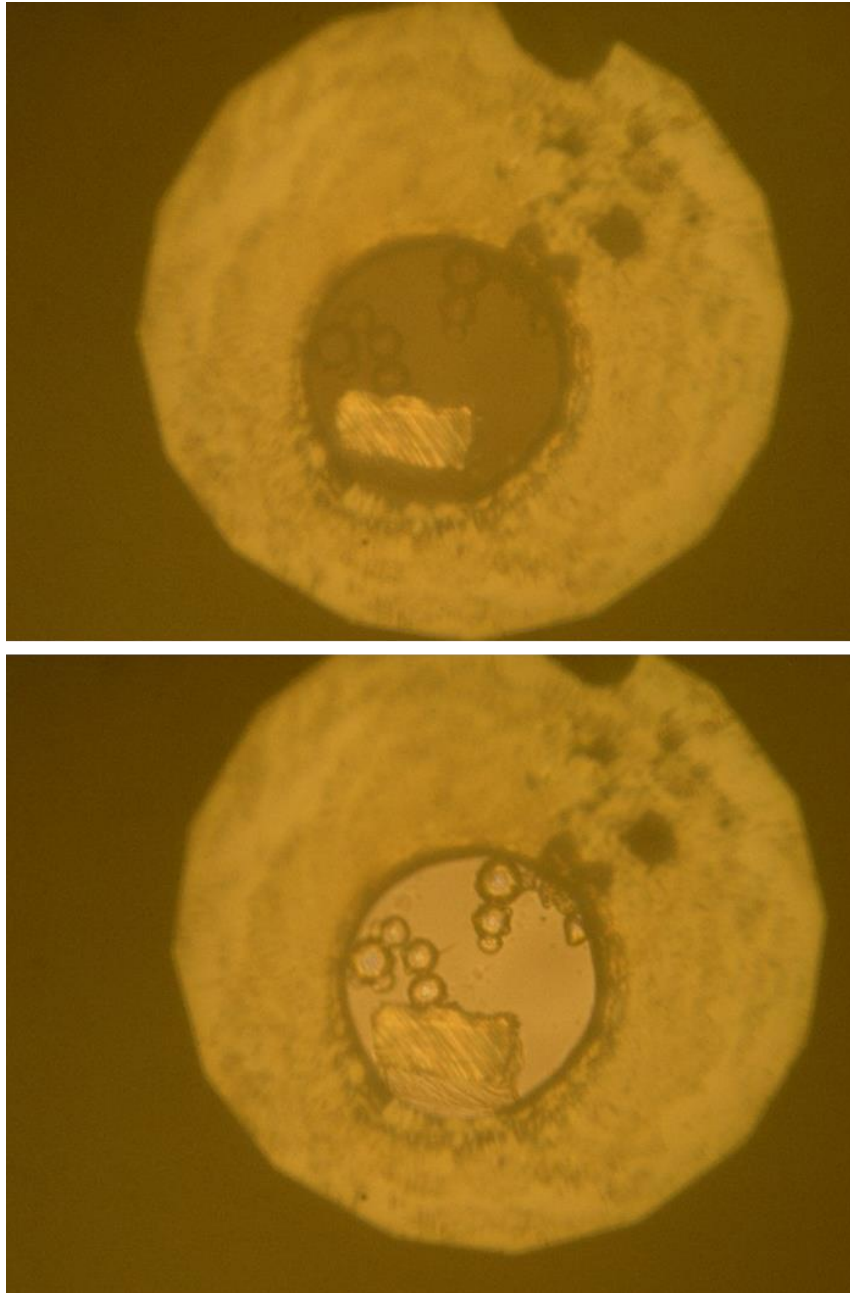


Figure 19. Damaged aluminum layer under 35 GPa. We found that the wrinkle on the sample always occurs parallel to the diagonal direction of the sample. The upper photo was taken using the upper light source, and the lower photo was taken using the lower light source. We can see the side of the transparent sample in the lower photo and we can find that the wrinkle not only distributes on the aluminum layer but also on the side of the sample; thus, we suggest this is an intrinsic property of siderite, which becomes very obvious when the siderite is placed with a -axis upward: the siderite might form the twin or might merely break along its cleavage under high pressure, making the aluminum along the a -axis become too tough to be probe by TDTR. This anomaly requires further investigations.

3.3. Results of thermal conductivity along c -axis

As shown in Fig. 20, the thermal conductivity along the c -axis increases from 2.5 W m⁻¹ K⁻¹ at the ambient condition to around 11 W m⁻¹ K⁻¹ at 35 GPa, but varies drastically during the spin transition between approximately 40 to 55 GPa. As the spin transition completes, the thermal conductivity increases slightly from around 7 W m⁻¹ K⁻¹ at 55 GPa to about 8 W m⁻¹ K⁻¹ at 67 GPa.

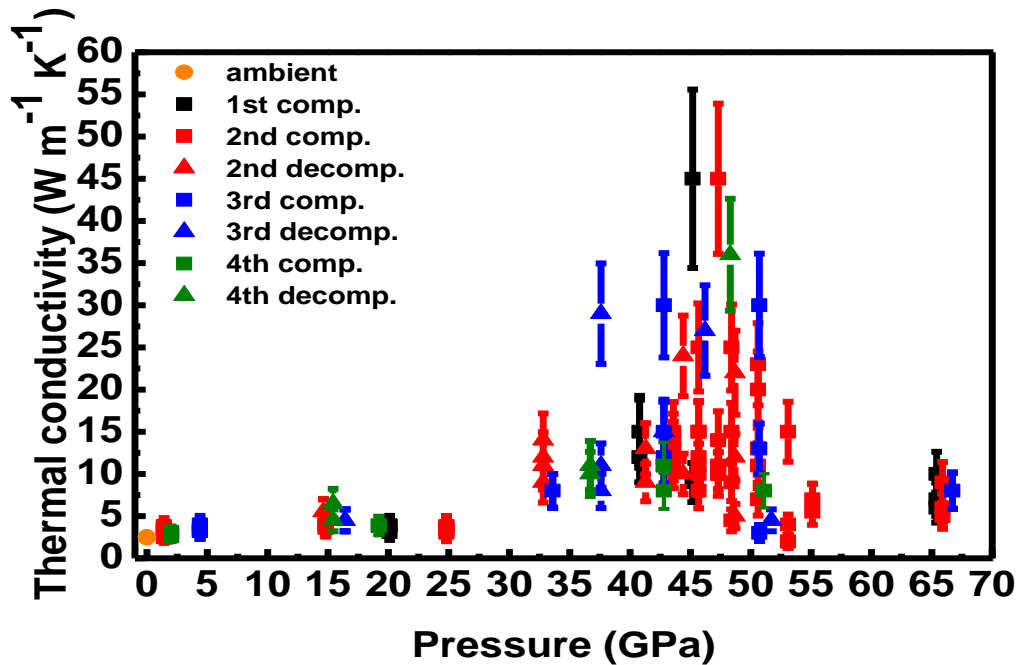


Figure 20. Pressure dependence of the thermal conductivity of siderite along c -axis. The orange circles represent the ambient data, and the squares and triangles represent the results during compression and decompression cycles, respectively. Each pressure point contains several data collected from different locations on the sample. The error bars were determined by the uncertainties contributed by the uncertainties in the parameters in our thermal model, which will be discussed in section 3.4. Note that there is no data for decompression cycle in the first run of measurement because the aluminum layer was damaged after compressed to 66 GPa. The data below 40 GPa and above 55 GPa are reasonably consistent among different runs of measurements: the thermal conductivity increases from 2.5 W m⁻¹ K⁻¹ at ambient condition to around 11 W m⁻¹ K⁻¹ at 35 GPa, and increases slightly from around 7 W m⁻¹ K⁻¹ at 55 GPa to around 8 W m⁻¹ K⁻¹ at 67 GPa. In contrast, the thermal conductivity during the spin transition (40-55 GPa) shows large variation.

The large variation of thermal conductivity during the spin transition results from the inhomogeneous spatial distribution of spin states within the siderite sample in the DAC. **Fig. 21** shows an example photograph of the siderite within a DAC under a mixed spin state at 47.3 GPa calibrated by the Ruby fluorescence, where the upper part of the sample (transparent part) is under the high spin state, and the lower part of the sample (dark part) is under the low spin state. As a result, the thermal conductivity at different locations of the sample varies considerably as shown in the **Fig. 21**.

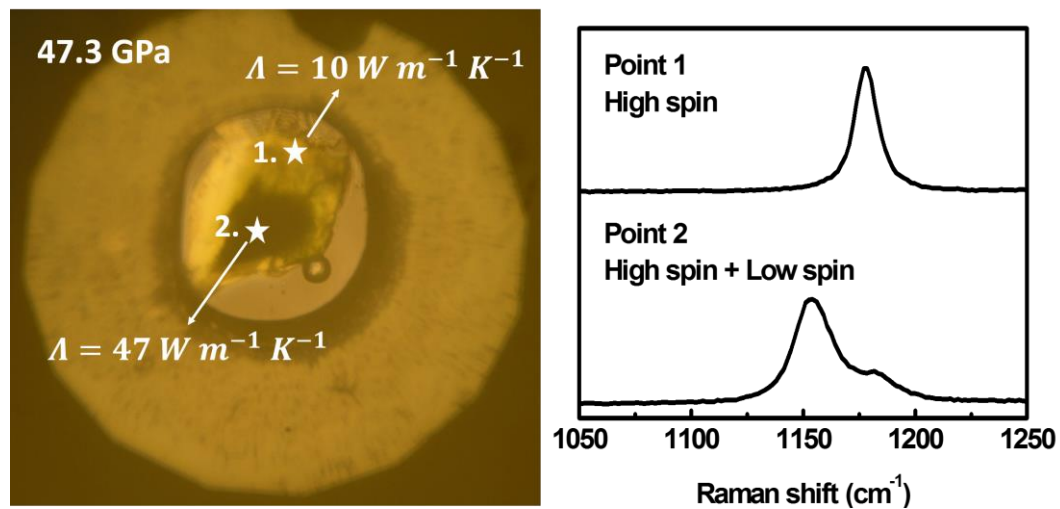


Figure 21. Inhomogeneous thermal conductivity caused by the spatially inhomogeneous distribution of spin state. The siderite under a mixed spin state within a DAC was under 47.3 GPa calibrated by Ruby fluorescence. The upper part with lighter color has lower thermal conductivity and its Raman spectrum shows that the spin transition does not occur yet, whereas the lower part looks darker and has higher thermal conductivity and its Raman spectrum shows that the spin transition already occurs.

To characterize the thermal conductivity of siderite during the spin transition between 40-55 GPa, we measured the thermal conductivity of a certain location on the

sample using TDTR and also collected its Raman spectrum, which enables us to figure out how the spin state influences the thermal conductivity. The characterization of the extent of spin state has been discussed in **section 2.2.2**. We plotted the thermal conductivity as a function of Normalized $A_{v_1}^{LS}/(A_{v_1}^{LS} + A_{v_1}^{HS})$ in **Fig. 22**. Interestingly, the thermal conductivity remains approximately a constant of $11 \text{ W m}^{-1} \text{ K}^{-1}$ as the Normalized $A_{v_1}^{LS}/(A_{v_1}^{LS} + A_{v_1}^{HS})$ is below 50%, and drastically increases with increasing Normalized $A_{v_1}^{LS}/(A_{v_1}^{LS} + A_{v_1}^{HS})$ until it reaches about 85%, followed by a sudden drop to about $5 \text{ W m}^{-1} \text{ K}^{-1}$ as the spin transition is going to complete.

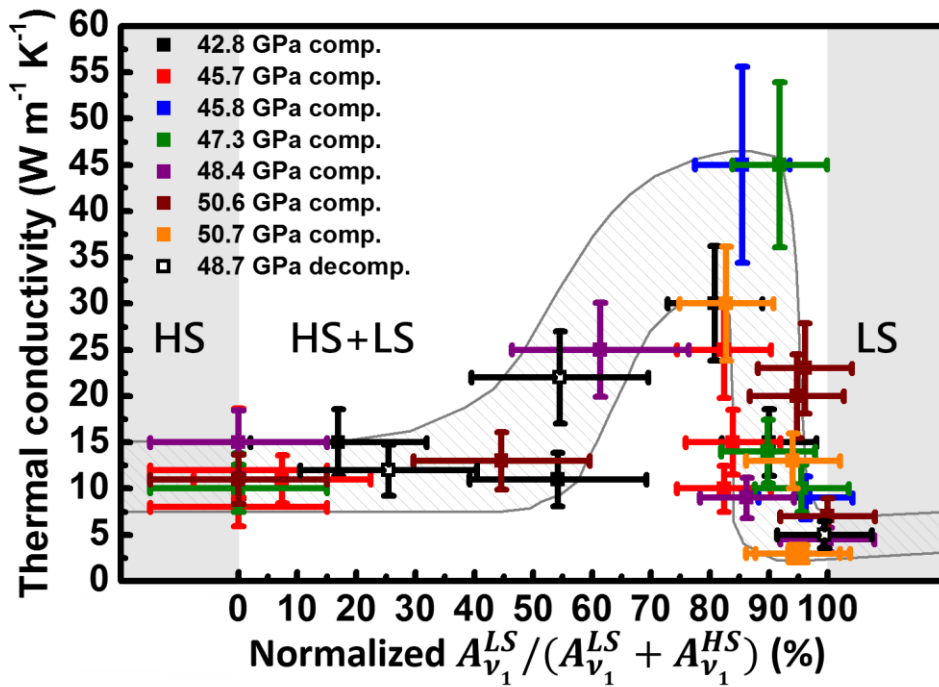


Figure 22. Thermal conductivity of siderite as a function of Normalized $A_{v_1}^{LS}/(A_{v_1}^{LS} + A_{v_1}^{HS})$. We analyzed the thermal conductivity data between 40-55 GPa in Fig. 20, and calculated their Normalized $A_{v_1}^{LS}/(A_{v_1}^{LS} + A_{v_1}^{HS})$. The thermal conductivity is almost a constant of $11 \text{ W m}^{-1} \text{ K}^{-1}$ while the normalized $A_{v_1}^{LS}/(A_{v_1}^{LS} + A_{v_1}^{HS})$ is below around 50%. The thermal conductivity suddenly increases by about three times to $45 \text{ W m}^{-1} \text{ K}^{-1}$ while the Normalized $A_{v_1}^{LS}/(A_{v_1}^{LS} + A_{v_1}^{HS})$ increases from 50% to 85%. Finally, the thermal conductivity suddenly drops to $5 \text{ W m}^{-1} \text{ K}^{-1}$ when the spin transition almost completes.

According to the cross line of the eyepiece of our microscope connected to the Raman spectrometer, a unit length is around 5 μm . Thus, in the Raman system, there are around 5 μm of uncertainties to posit the location probed by the TDTR. The error of Normalized $A_{\nu_1}^{LS} / (A_{\nu_1}^{LS} + A_{\nu_1}^{HS})$ under mixed-spin state was estimated by observing the Raman spectra of sample shifting per 5 μm and comparing the difference between the Raman spectra of two neighboring locations. We defined a factor, R, as $A_{\nu_1}^{LS} / (A_{\nu_1}^{LS} + A_{\nu_1}^{HS})$. We characterized the values of Rs at different sampling locations among the sample. We found that the differences in R between two neighboring locations are typically 15% while the R is lower than 65%, and typically 8% when R is greater than 65%. See **Fig. 23**. Thus, in **Fig. 23**, the uncertainty in each line (table shown in the right panel) is estimated to be 15% and 8% for Rs lower and greater than 65%, respectively.

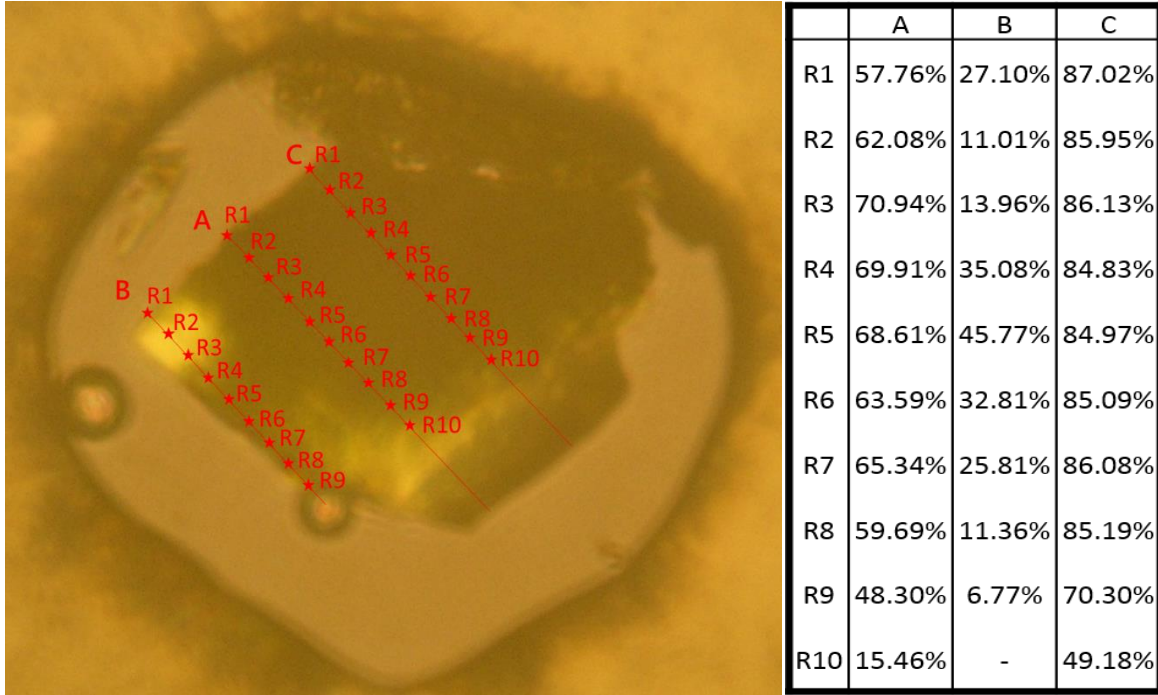


Figure 23. Estimation of error bars of Normalized $A_{v_1}^{LS}/(A_{v_1}^{LS} + A_{v_1}^{HS})$. The optical photograph shows the sampling positions of Raman spectroscopy under a mixed spin state at 45.6 GPa. There are three sampling lines: A, B, and C. Each line contains 9-10 points defined as for R1-R10 with a spatial interval of 5 μm . R is defined as $A_{v_1}^{LS}/(A_{v_1}^{LS} + A_{v_1}^{HS})$. The values of R1-R10 are shown in the table on the right-hand side. Because the beam size of TDTR is around 14 μm -diameter, which contains around 3 points of the sampling points in this graph, we compared the difference between two neighboring Rs to evaluate the uncertainties of the Normalized $A_{v_1}^{LS}/(A_{v_1}^{LS} + A_{v_1}^{HS})$. The difference between two neighboring Rs is typically around 15% as the $A_{v_1}^{LS}/(A_{v_1}^{LS} + A_{v_1}^{HS})$ is lower than 65%, and typically around 8% as the $A_{v_1}^{LS}/(A_{v_1}^{LS} + A_{v_1}^{HS})$ is greater than 65%, respectively. Thus, the error bar of Normalized $A_{v_1}^{LS}/(A_{v_1}^{LS} + A_{v_1}^{HS})$ in Fig. 22 is estimated to be 15% as the Normalized $A_{v_1}^{LS}/(A_{v_1}^{LS} + A_{v_1}^{HS})$ is lower than 65% and 8% as the Normalized $A_{v_1}^{LS}/(A_{v_1}^{LS} + A_{v_1}^{HS})$ is greater than 65%

According to **Figs. 20-22**, we can make a small conclusion: it is better to express the thermal conductivity of siderite at 40-55 GPa as a function of Normalized $A_{v_1}^{LS}/(A_{v_1}^{LS} + A_{v_1}^{HS})$ or the fraction of low spin state rather than pressure, since the thermal conductivity has strong dependence to the fraction of low spin state and the spatial distribution of spin state is rarely homogeneous.

The mechanisms causing this thermal conductivity anomaly remains unknown. However, Morton and Lewis' research [48] could be a potential clue. Morton and Lewis [50] showed that the spin momentum of iron impurities interferes the phonons' movement in the magnesium oxide crystal; as a result, the thermal conductivity of magnesium oxide is suppressed by the spin momentum. According to this theory, the greater the spin momentum is, the lower the thermal conductivity is. This phenomenon is termed resonant spin-phonon scattering. Similarly, siderite has the same Fe-O octahedra as (Mg, Fe)O, and therefore, the thermal conductivity increases drastically upon the onset of spin transition might be because the resonant spin-phonon scattering starts to diminish due to the decrease of spin momentum caused by the spin transition. However, this theory fails to explain the drastic drop of thermal conductivity as the spin transition completes (spin momentum=0). The detailed mechanisms require further investigations.

3.4. Uncertainties of TDTR

The errors of thermal conductivity in this study were typically contributed by the uncertainty of each factor in the thermal model. We estimated the errors by defining a new parameter called sensitivity parameter, $S_{\alpha} = \frac{\partial \ln(-\frac{V_{in}}{V_{out}})}{\partial \ln \alpha} = \frac{\Delta \text{ratio}/\text{ratio}}{\Delta \alpha/\alpha}$, where α is one of any parameters of the thermal model (e.g., thermal conductance,

heat capacity of each layer, etc.). To calculate the S_α , we typically raised α by 10% and observed the variation of ratio, which is the $-V_{in}/V_{out}$ mentioned in **section 2.4**. For example, if the ratio increases by 6% as α raises by 10%, and then the S_α is (6%/10%=0.6). If the ratio decreases by 4% as α raises by 10%, the S_α is -0.4, and then the details to calculate α is shown in the figures below (**Fig. 24 and Fig. 25**).

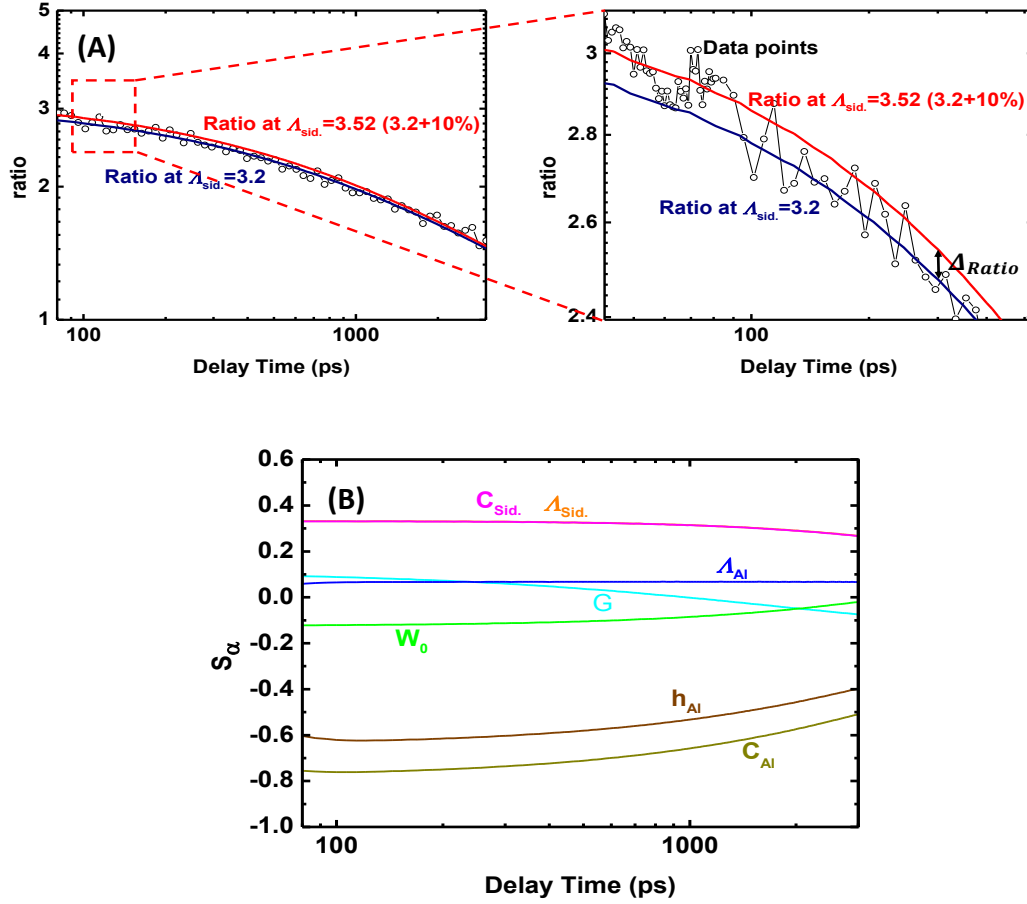
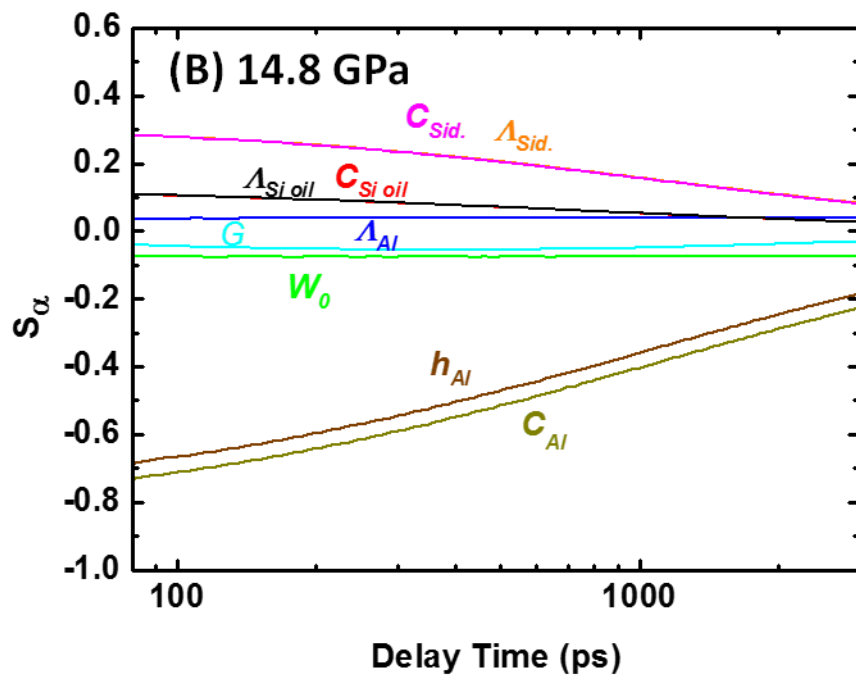
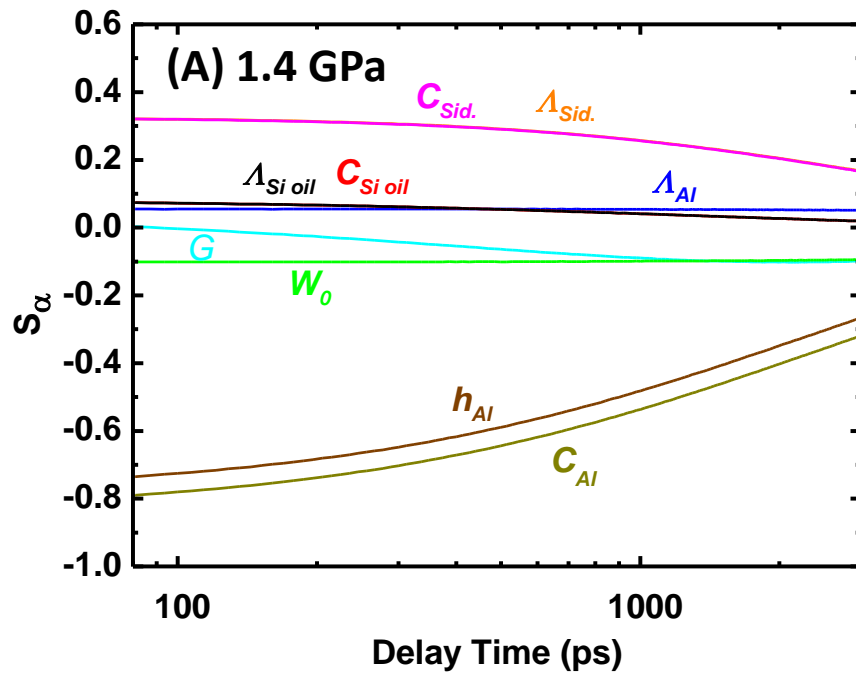
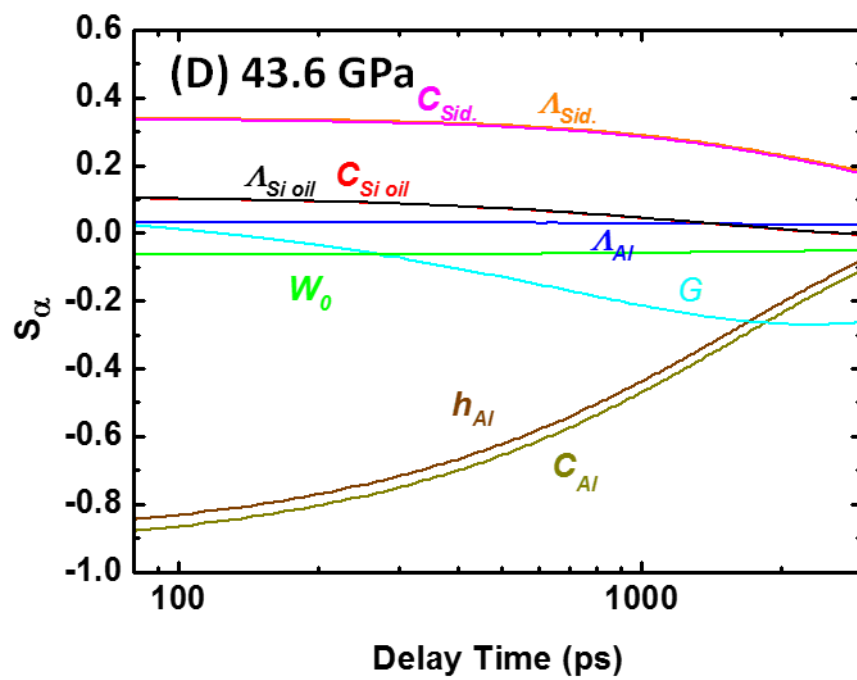
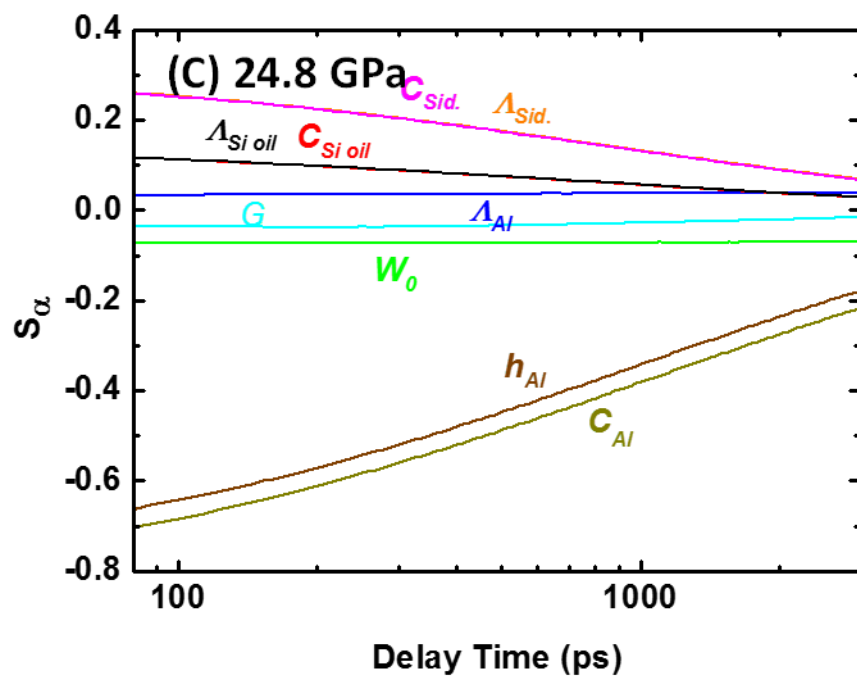


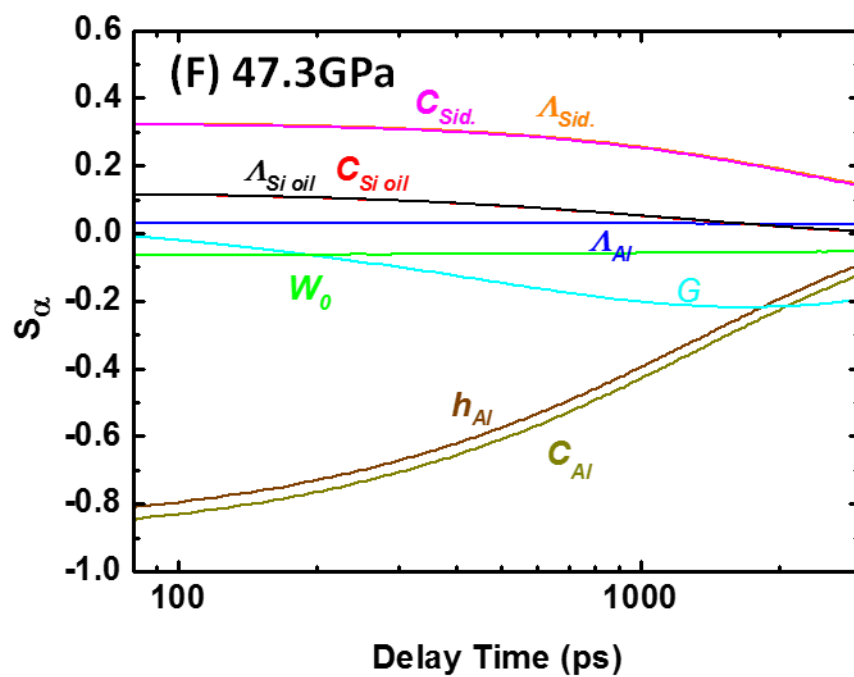
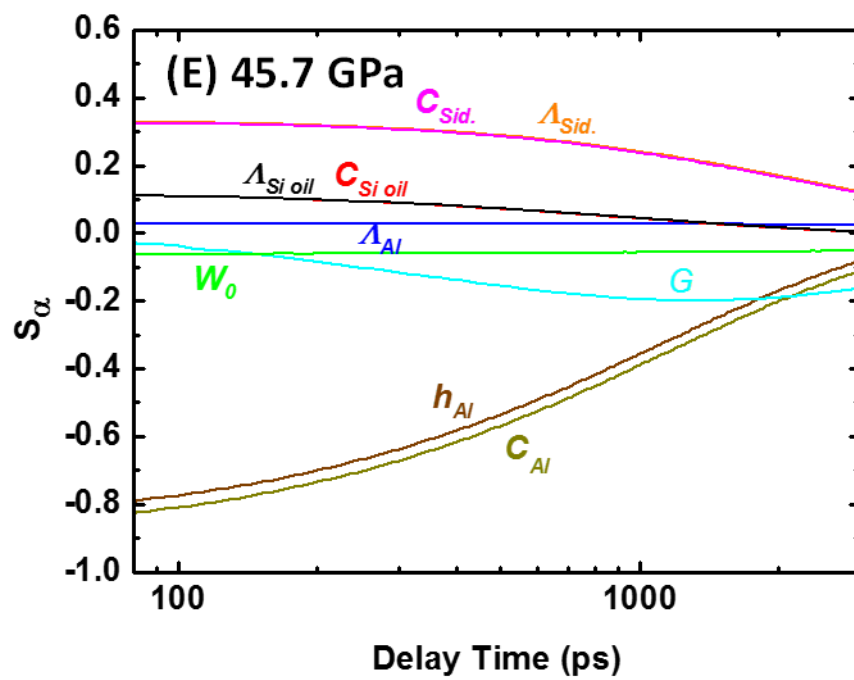
Figure 24. Process to figure out the sensitivity parameters under ambient condition. (A) The ratio of raw data points is shown as the open circles. For example, a blue curve with $A_{sid}=3.2$ was the plot to fit the data point. Then we increased A_{sid} into 3.52 (increase by 10%) to run the model again, and we obtained the red line showing slightly increased ratio. The gap between the blue line and the red line is defined as Δ_{ratio} . Then the sensitivity parameter was derived from A_{sid} .

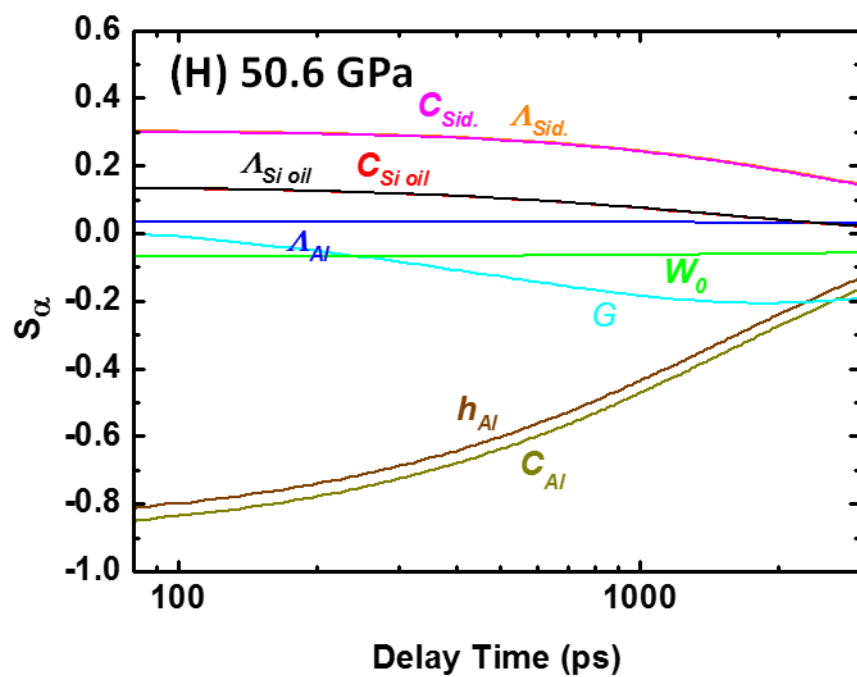
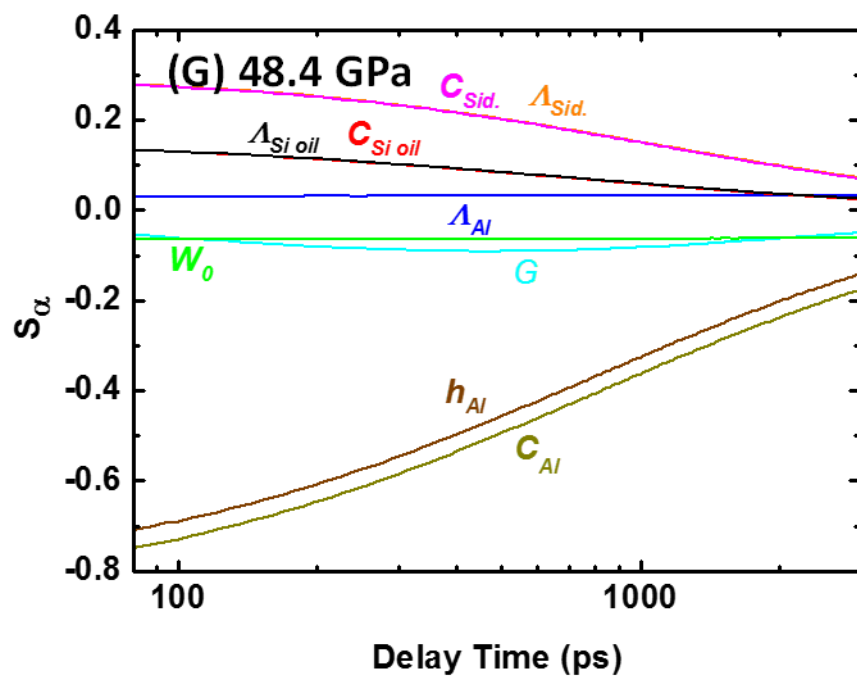
calculated by $S_{A_{sid}} = \frac{\Delta_{ratio}/ratio}{\Delta A_{sid}/A_{sid}}$, since the $\Delta A_{sid}/A_{sid}$ was already intentionally set to be 10%. The

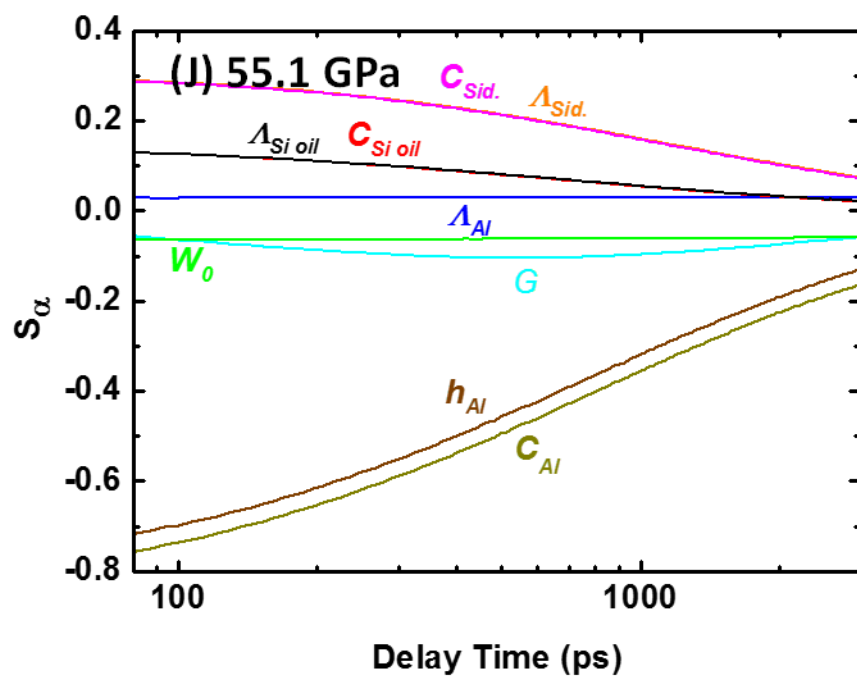
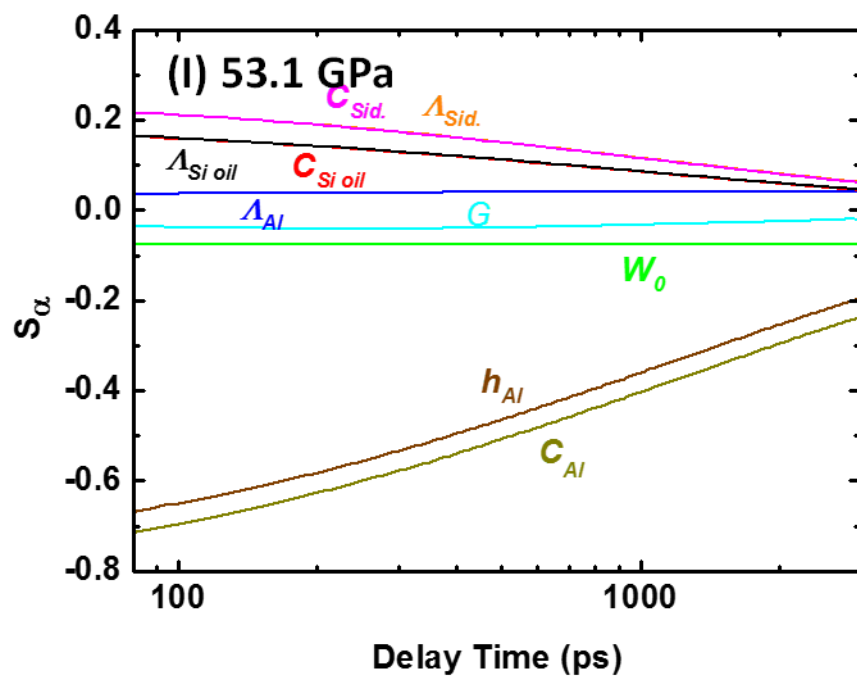
variation of $S_{A_{sid}}$ as a function of delay time could easily to be calculated. (B) By repeating the aforementioned process, we plotted the sensitivity of each parameter in the thermal model. The figure shows the sensitivity factor contributed by each parameter at ambient condition (sample is exposed to the air instead of being confined within the DAC). According to the absolute value of these curves, we can easily find that the dominant parameters determining the uncertainties of the data are h_{Ai} and C_{Ai} , whereas the ratio is very insensitive to some terms such as W_0 (diameter of beam spot) or A_{Ai} . Note that the C_{sid} and A_{sid} are always close or even overlap with each other. A similar result also occurs while the $C_{si\ oil}$ and $A_{si\ oil}$ are added into our model when the sample is loaded into the DAC. There is no surprise to this consequence since the thermal effusivity is defined as $e = \sqrt{AC}$, the contribution from both terms is almost equal.











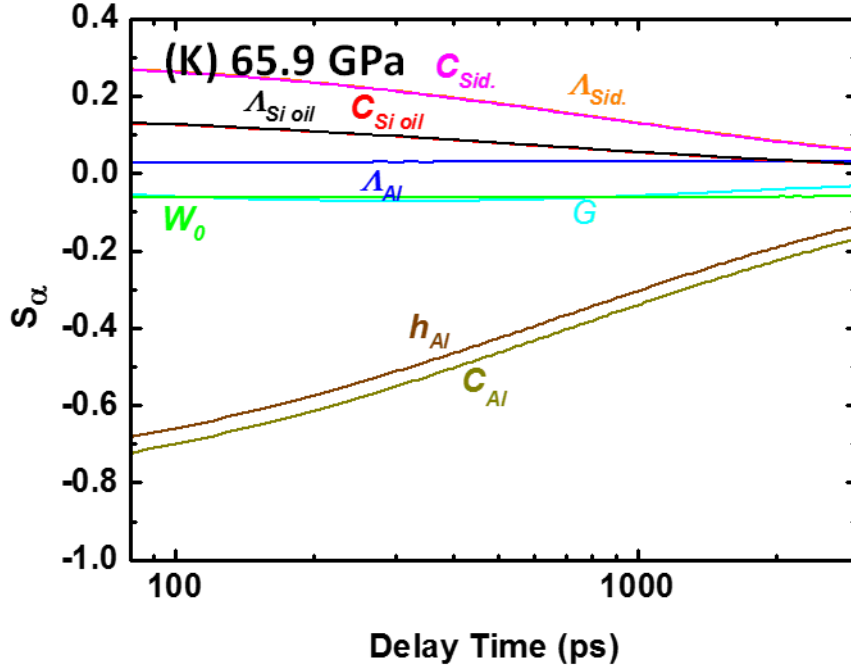


Figure 25. Sensitivity parameters under several pressures (A)-(K). These results are very similar to the conclusions drawn from the ambient condition. The only difference is that the $C_{Si\ oil}$ and $A_{Si\ oil}$ were added into these diagrams to express the pressure medium layer. The contributions from $C_{Si\ oil}$ and $A_{Si\ oil}$ are almost equal since e is defined as $\sqrt{\Lambda C}$.

The error propagated by the uncertainty of each parameter was derived by comparing those sensitivity factors. First of all, we averaged all of the sensitivity parameters within the delay time from 80 ps to 1000 ps. Secondly, we calculated $S_\alpha/S_{A_{Sid.}}$, which means the relative sensitivity contributing to the error of $A_{Sid.}$. The idea is to estimate how much error was contributed to $A_{Sid.}$ by the variation of α . The details of calculation processes are described as follows.

$$S_\alpha = \frac{\Delta ratio - ratio}{\Delta \alpha / \alpha} \quad (10)$$

$$S_{A_{Sid.}} = \frac{\Delta ratio - ratio}{\Delta \Lambda_{Sid.} / \Lambda_{Sid.}} \quad (11)$$

$$\frac{S_{A_{Sid.}}}{S_\alpha} = \frac{\Delta \alpha / \alpha}{\Delta \Lambda_{Sid.} / \Lambda_{Sid.}} \Rightarrow \frac{\Delta \Lambda_{Sid.}}{\Lambda_{Sid.}} = \frac{S_\alpha}{S_{A_{Sid.}}} \left(\frac{\Delta \alpha}{\alpha} \right) \quad (12)$$

Hence, for example, if α represents the thickness of the aluminum layer, the formula can be written as $\frac{S_{h_{Al}}}{S_{A_{sid}}}$, which is typically around 2.5; if the uncertainty of aluminum thickness is 10%, the $\frac{\Delta A_{sid}}{A_{sid}}$ is 25%, meaning that the uncertainty of aluminum thickness contributes 25% of error into the thermal conductivity measurements of siderite. The total error propagated by those parameters was calculated by the formula, $\sqrt{\sum[\frac{S_{\alpha}}{S_{A_{sid}}}(\frac{\Delta\alpha}{\alpha})]^2}$. Thus, for instance, the estimated uncertainties of C_{Al} , $C_{si\ oil}$, C_{sid} , h_{Al} , A_{Al} , $A_{si\ oil}$, G , W_0 are typically 5%, 5%, 10%, 10%, 10%, 5%, 10%, and 3%, respectively, and the calculated $\frac{S_{\alpha}}{S_{A_{sid}}}$ of each term at 14.8 GPa is -2.516, 0.352, 0.999, -0.237, -2.315, 0.174, 0.352, -0.348, respectively. The uncertainties propagate

$$\sqrt{[5\% \times (-2.516)]^2 + [5\% \times 0.352]^2 + [10\% \times 0.999]^2 + [10\% \times (-0.237)]^2 + [10\% \times (-2.315)]^2 + [5\% \times 0.174]^2 + [10\% \times 0.352]^2 + [3\% \times (-0.348)]^2} \approx$$

28.582% of error to our result. The tables below (**Table 4 and 5**) are examples showing the average sensitivity parameters within 80-1000 ps and the error estimated under ambient condition and pressure points of A~K of **Fig. 25**.

Pressure (GPa)	$S_{C_{Al}}$	$S_{C_{Si\ oil}}$	$S_{C_{Sid.}}$	S_G	$S_{h_{Al}}$	$S_{\Lambda_{Al}}$	$S_{\Lambda_{Si\ oil}}$	$S_{\Lambda_{Sid.}}$	S_{W_0}
0	-0.630	-	0.337	0.005	-0.561	0.066	-	0.337	-0.122
1.4	-0.666	0.057	0.294	-0.052	-0.611	0.055	0.057	0.295	-0.101
14.8	-0.551	0.077	0.217	-0.052	-0.507	0.038	0.077	0.219	-0.0763
24.8	-0.524	0.082	0.189	-0.034	-0.484	0.036	0.082	0.190	-0.072
43.6	-0.686	0.076	0.315	-0.103	-0.653	0.030	0.077	0.320	-0.062
45.7	-0.609	0.078	0.290	-0.130	-0.575	0.028	0.079	0.293	-0.060
47.3	-0.645	0.086	0.294	-0.120	-0.610	0.030	0.087	0.297	-0.062
48.4	-0.538	0.092	0.214	-0.084	-0.500	0.031	0.093	0.215	-0.065
50.6	-0.669	0.107	0.277	-0.104	-0.632	0.034	0.108	0.279	-0.067
53.1	-0.542	0.120	0.161	-0.038	-0.498	0.039	0.121	0.162	-0.076
55.1	-0.540	0.089	0.224	-0.094	-0.502	0.030	0.089	0.226	-0.063
65.9	-0.509	0.087	0.195	-0.067	-0.470	0.029	0.088	0.196	-0.063

Table 4. Averaged sensitivity parameters contributed by parameters of thermal model. We averaged the curve shown in Fig. 25 from 80 ps to 1000 ps to derive the general sensitivity parameters of all of the factors for the pressures listed in the Table. Note that, as the Fig. 25 has shown, the $S_{C_{Si\ oil}}$ is close to $S_{\Lambda_{Si\ oil}}$ and $S_{C_{Sid.}}$ is close to $S_{\Lambda_{Sid.}}$ respectively. The ambient datum does not have silicone oil because the ambient sample is exposed to the air rather than confined into the cell.

Pressure (GPa)	$\frac{S_{C_{Al}}}{S_{\Lambda_{Sid.}}}$	$\frac{S_{C_{Si\ oil}}}{S_{\Lambda_{Sid.}}}$	$\frac{S_{C_{Sid.}}}{S_{\Lambda_{Sid.}}}$	$\frac{S_G}{S_{\Lambda_{Sid.}}}$	$\frac{S_{h_{Al}}}{S_{\Lambda_{Sid.}}}$	$\frac{S_{\Lambda_{Al}}}{S_{\Lambda_{Sid.}}}$	$\frac{S_{\Lambda_{Si\ oil}}}{S_{\Lambda_{Sid.}}}$	$\frac{S_{W_0}}{S_{\Lambda_{Sid.}}}$	Estimated Error (%)
0	-1.869	-	1.000	0.015	-1.665	0.196	-	-0.362	8.180
1.4	-2.258	0.193	0.997	-0.176	-2.071	0.186	0.193	-0.342	25.792
14.8	-2.516	0.352	0.999	-0.237	-2.315	0.174	0.352	-0.348	28.582
24.8	-2.758	0.432	0.995	-0.179	-2.547	0.189	0.432	-0.379	31.090
43.6	-2.144	0.238	0.984	-0.322	-2.041	0.094	0.241	-0.194	25.426
45.7	-2.080	0.266	0.990	-0.444	-1.964	0.096	0.270	-0.205	24.926
47.3	-2.172	0.290	0.990	-0.404	-2.054	0.101	0.293	-0.209	25.797
48.4	-2.502	0.428	0.995	-0.391	-2.326	0.144	0.433	-0.302	28.922
50.6	-2.395	0.383	0.992	-0.372	-2.263	0.122	0.387	-0.240	28.059
53.1	-3.346	0.741	0.994	-0.235	-3.074	0.241	0.747	-0.469	37.445
55.1	-2.389	0.394	0.991	-0.416	-2.221	0.133	0.394	-0.279	27.785
65.9	-2.597	0.444	0.995	-0.342	-2.398	0.148	0.449	-0.321	29.680

Table 5. Estimated errors contributed by the sensitivity parameters of thermal model. The table

of the $\frac{S_\alpha}{S_{\Lambda_{Sid.}}}$ and the error were calculated by the above-mentioned approach. The uncertainties of all of the factors of the ambient condition were assumed to be 3% because they were easy to be measured accurately under ambient. Except for the ambient condition, the estimated uncertainties of these factors, C_{Al} , $C_{Si\ oil}$, $C_{sid.}$, h_{Al} , Λ_{Al} , $\Lambda_{Si\ oil}$, G , W_0 , were typically 5%, 5%, 10%, 10%, 10%, 5%, 10%, and 3% respectively. The most uncertain terms, $C_{sid.}$, G , h_{Al} , and Λ_{Al} , were empirically assumed to be 10% of uncertainty. These factors are typically assumed to be constants when pressure arise such as $C_{sid.}$ and Λ_{Al} , or can only be fitted by trial and error in the model, for instance, G , or cannot be accurately measured but can only be derived by rough calculation like the h_{Al} . The second category contains the C_{Al} , $C_{Si\ oil}$ and $\Lambda_{Si\ oil}$. These terms were obtained by theoretical calculations or from literature with assumed uncertainties of 5%. The final category is the W_0 ; since the spot size is part of our apparatuses set up, we are almost certain that it will not change, it is assumed to be 3%. By the formula, $\sqrt{\sum[\frac{S_\alpha}{S_{\Lambda_{Sid.}}}(\frac{\Delta\alpha}{\alpha})]^2}$, the errors are shown in the last column of the table.

CHAPTER 4

SUMMARY

We combined diamond anvil cell with Raman spectroscopy and time-domain thermoreflectance to study the thermal conductivity of siderite across the spin transition. We found that the thermal conductivity of siderite drastically increases by three times to $45 \text{ W m}^{-1} \text{ K}^{-1}$ with the fraction of low spin iron and drops eight times to $5 \text{ W m}^{-1} \text{ K}^{-1}$ as the spin transition almost completes. Such violent thermal conductivity variation across a narrow pressure range has never been observed in other minerals.

This thermal conductivity anomaly implies that if the siderite can be transported to a depth of 1100 to 1500 km by the subduction of slabs, the large variation of thermal conductivity may induce local heat flux anomaly and further cause local temperature anomaly. For example, in the spin transition depth, the siderite allows greater heat flux to flow through it during the spin transition due to its high thermal conductivity, causing a local high-temperature area. In the depth slightly deeper than spin transition depth, the siderite suddenly becomes an insulator after spin transition completes, and therefore, this thermal conductivity drop may cause a local low-temperature area or maintain an existed high-temperature block form cooling down. However, these two contradictory thermal properties (thermal conductor and insulator) will occur one after another within narrow pressure range (tens of km).

Such local temperature anomalies in the temperature profile would further influence the stability of minerals in these regions. If the stability of mineral phases is disturbed by these temperature anomalies caused by siderite, the mineral phases at depth of 1100 to 1500 km may become more complex than what we thought. Therefore, the thermal conductivity anomaly of siderite across spin transition provides a new insight into our concepts of temperature profile and thermal properties of lower mantle.

REFERENCES

- [1] R. Dasgupta, and M.M. Hirschmann, "The deep carbon cycle and melting in Earth's interior", Earth and Planetary Science Letters, Vol 298, 1, 2010.
- [2] C. Biellmann, P. Gillet, F. Guyot, J. Peyronneau, and B. Reynard, "Experimental evidence for carbonate stability in the Earth's lower mantle", Earth and Planetary Science Letters, Vol 118, 31, 1993.
- [3] P. Gillet, "Stability of magnesite (MgCO_3) at mantle pressure and temperature conditions: A Raman spectroscopic study", American Mineralogist, Vol 78, 1328, 1993.
- [4] A.R. Oganov, S. Ono, Y. Ma, C.W. Glass, and A. Garcia, "Novel high-pressure structures of MgCO_3 , CaCO_3 and CO_2 and their role in Earth's lower mantle", Earth and Planetary Science Letters, Vol 273, 38, 2008.
- [5] B. Lavina, P. Dera, R.T. Downs, V. Prakapenka, M. Rivers, S. Sutton, and M. Nicol, "Siderite at lower mantle conditions and the effects of the pressure-induced spin-pairing transition", Geophysical Research Letters, Vol 36, L23306, 2009.
- [6] J.F. Lin, J. Liu, C. Jacobs, and V.B. Prakapenka, "Vibrational and elastic properties of ferromagnesite across the electronic spin-pairing transition of iron", American Mineralogist, Vol 97, 583, 2012.
- [7] S.S. Lobanov, A.F. Goncharov, and K.D. Litasov, "Optical properties of siderite (FeCO_3) across the spin transition: Crossover to iron-rich carbonates in the lower mantle", American Mineralogist, Vol 100, 1059, 2015.
- [8] S. Fu, J. Yang, and J.F. Lin, "Abnormal elasticity of single-crystal magnesiosiderite across the spin transition in Earth's lower mantle". Physical Review Letter, Vol 118, 036402, 2017.
- [9] K.D. Litasov, A. Shatskiy, P.N. Gavryushkin, I.S. Sharygin, P.I. Dorogokupets, A.M. Dymshits, E. Ohtani, Y. Higo, and K. Funakoshi, "P–V–T equation of state of siderite to 33 GPa and 1673K", Physics of the Earth and Planetary Interiors, Vol 224, 83, 2013.
- [10] J.F. Lin, and A. Wheat, "Electronic spin transition of iron in the Earth's lower mantle", Hyperfine Interactions, Vol 207, 81, 2011.
- [11] K. Cornelis, and S.H. Cornelius, Jr., Manual of Mineralogy, 1985, John Wiley & Sons, New York, 1985.
- [12] P.W. Bridgman, "The Thermal conductivity and compressibility of several rocks under high pressures", American Journal of Science C, Vol 7, 81, 1924.

- [13] F.R. Boyd, and J.L. England, "Apparatus for phase-equilibrium measurements at pressures up to 50 kilobars and temperatures up to 1750°C", Jouranal of Geophysical Research, Vol 65, 741, 1960.
- [14] H. Fujisawa, N. Fujii., H. Mizutani, H. Kanamori, and S. Akimoto, "Thermal diffusivity of Mg₂SiO₄, Fe₂SiO₄, and NaCl at high pressures and temperatures", Journal of Geophysical Research, Vol 73, 4727, 1968.
- [15] T. Katsura, "Thermal diffusivity of olivine under upper mantle conditions", Geophysical Journal International, Vol 122, 63, 1995.
- [16] T. Katsura, "Thermal diffusivity of silica glass at pressures up to 9 GPa", Physics and Chemistry of Minerals, Vol 20, 201, 1993.
- [17] L. Dubrovinsky, N. Dubrovinskaia, E. Bykova, M. Bykov, V. Prakapenka, C. Prescher, K. Glazyrin, H.P. Liermann, M. Hanfland, M. Ekholm, Q. Feng, L.V. Pourovskii, M.I. Katsnelson, J.M. Wills, and I.A. Abrikosov, "The most incompressible metal osmium at static pressures above 750 gigapascals", Nature, Vol 525, 226, 2015.
- [18] P. Beck, A.F. Goncharov, V.V. Struzhkin, B. Militzer, H.K. Mao, and R.J. Hemley, "Measurement of thermal diffusivity at high pressure using a transient heating technique", Applied Physics Letters, Vol 91, 181914, 2007.
- [19] W.P. Hsieh, "Thermal conductivity of methanol-ethanol mixture and silicone oil at high pressures", Journal of Applied Physics, Vol 117, 235901, 2015.
- [20] W.P. Hsieh, "Testing theories for thermal transportation using high pressure", University of Illinois at Urbana-Champaign, Degree of Doctor of Philosophy in Physics, 2011.
- [21] W.P. Hsieh, B. Chen, J. Li, P. Keblinski, and D.G. Cahill, "Pressure tuning of the thermal conductivity of the layered muscovite crystal", Physical Review B, Vol 80, 180302, 2009.
- [22] Y.Y. Chang, W.P. Hsieh, E. Tan, and J. Chen, "Hydration-reduced lattice thermal conductivity of olivine in Earth's upper mantle", Proceeding of the National Academy of Science of the United States of America, Vol 114, 4078, 2017.
- [23] S.J.B. Reed, Electron microprobe analysis and scanning electron microscopy in Geology, Cambridge University Press, Cambridge, 2005.
- [24] V. Randle, "Electron backscatter diffraction: Strategies for reliable data acquisition and processing", Materials Characterization, Vol 60, 913, 2009.
- [25] S. Nishikawa, and S. Kikuchi, "The diffraction of cathode rays by calcite", Nature, Vol 122, 475, 1928.
- [26] C.V. Raman, and K.S. Krishinan, "A new type of secondary radiation", Nature, Vol 121, 501, 1928.

- [27] G.A. Farfan, S. Wang, H. Ma, R. Caracas, and W.L. Mao, "Bonding and structural changes in siderite at high pressure", American Mineralogist, Vol 97, 1421, 2012.
- [28] V. Cerantola, C. McCammon, I. Kupaenko, I. Kantor, C. Marini, M. Wilke, L. Ismailova, N. Solopova, A. Chumakov, S. Pascarelli, and L. Dubrovinsky, "High-pressure spectroscopic study of siderite (FeCO₃) with a focus on spin crossover", American Mineralogist, Vol 100, 2670, 2015.
- [29] C. Weis, C. Sternemann, V. Cerantola, C.J. Sahle, G. Spiekermann, M. Harder, Y. Forov, A. Kononov, R. Sakrowski, H. Yavaş, M. Tolan, and M. Wilke, "Pressure driven spin transition in siderite and magnesiosiderite single crystals", Scientific Reports, Vol 7, 16526, 2017.
- [30] A. Mattila, T. Pylkkänen, J.P. Rueff, S. Huotari, G. Vankó, M. Hanfland, M. Lehtinen, and K. Hämäläinen, "Pressure induced magnetic transition in siderite FeCO₃ studied by X-ray emission spectroscopy", Journal of Physics: Condensed Matter, Vol 19, 386206, 2007.
- [31] J.D. Barnett, S. Block, and G.J. Piermarini, "An optical fluorescence system for quantitative pressure measurement in the diamond-anvil cell", Review of Scientific Instruments, Vol 44, 1, 1973.
- [32] H.K. Mao, J. Xu, and P.M. Bell, "Calibration of the ruby pressure gauge to 800 kbar under quasi-hydrostatic conditions", Journal of Geophysical Research, Vol 91, 4673, 1986.
- [33] S. Klotz, J.C. Chervin, P. Munsch, and G.L. Marchand, "Hydrostatic limits of 11 pressure transmitting media", Journal of Physics D: Applied Physics, Vol 42, 075413, 2009.
- [34] K. Kang, Y.K. Koh, C. Chiritescu, X. Zheng, and D.G. Cahill, "Two-tint pump-probe measurements using a femtosecond laser oscillator and sharp-edged optical filters", Review of Scientific Instruments, Vol 79, 114901, 2008.
- [35] W.P. Binnie, "Calculation of the mean Debye temperature of cubic crystals", Physical Review, Vol 103, 579, 1956.
- [36] G.A. Farfan, E. Boulard, S. Wang, and W.L. Mao, "Bonding and electronic changes in rhodochrosite at high pressure", American Mineralogist, Vol 98, 1817, 2013.
- [37] C. Bercegeay, and S. Bernard, "First-principles equations of state and elastic properties of seven metals", Physical Review B, Vol 72, 214101, 2005.
- [38] R.A. Robie, H.T. Haselton, Jr., and B.S. Hemingway, "Heat capacities and entropies of rhodochrosite (MnCO₃) and siderite (FeCO₃) between 5 and 600 K", American Mineralogist, Vol 69, 349, 1984.

- [39] D.G. Cahill, "Analysis of heat flow in layered structures for time-domain thermoreflectance", Review of Scientific Instruments, Vol 75, 5119, 2004.
- [40] W.D. Bischoff, S.K. Sharma, and F.T. Mackenzie, "Carbonate ion disorder in synthetic and biogenic magnesian calcites: a Raman spectral study", American Mineralogist, Vol 70, 581, 1985.
- [41] B. Lavina, P. Dera, R.T. Downs, W. Yang, S. Sinogeikin, Y. Meng, G. Shen, and D. Schiferl, "Structure of siderite FeCO_3 to 56 GPa and hysteresis of its spin-pairing transition", Physical Review B, Vol 82, 064110, 2010.
- [42] B. Lavina, P. Dera, R.T. Downs, O. Tschauer, W. Yang, O. Shebanova, and G. Shen, "Effect of dilution on the spin pairing transition in rhombohedral carbonates", High Pressure Research, Vol 30, 224, 2010.
- [43] T. Nagai, T. Ishido, Y. Seto, D. Nishio-Hamane, N. Sata, and K. Fujino, "Pressure-induced spin transition in FeCO_3 -siderite studied by X-ray diffraction measurements", Journal of Physics: Conference Series, Vol 215, 012002, 2010.
- [44] Y. Fei, L. Zhang, A. Corgne, H. Watson, A. Ricolleau, Y. Meng, and V. Prakapenka, "Spin transition and equations of state of (Mg, Fe)O solid solutions", Geophysical Research Letters, Vol 34, L17307, 2007.
- [45] J. Müller, I. Efthimiopoulos, S. Jahn, and M. Koch-Müller, "Effect of temperature on the pressure-induced spin transition in siderite and iron-bearing magnesite: a Raman spectroscopy study", European Journal of Mineralogy, Vol 29, 785, 2017.
- [46] J. Liu, J.F. Lin, Z. Mao, and V.B. Prakapenka, "Thermal equation of state and spin transition of magnesiosiderite at high pressure and temperature", American Mineralogist, Vol 99, 84, 2014.
- [47] M. Merlini, M. Hanfland, and M. Gemmi, "The MnCO_3 -II high-pressure polymorph of rhodocrosite", American Mineralogist, Vol 100, 2625, 2015.
- [48] J. Zhang, I. Martinez, F. Guyot, and J.R. Richard, "Effects of Mg-Fe^{2+} substitution in calcite-structure carbonates: Thermoelastic properties", American Mineralogist, Vol 83, 280, 1998.
- [49] R.G. Dandrea, and N.W. Ashcroft, "High pressure as a probe of electron structure: Aluminum", Physical Review B, Vol 32, 6936, 1985.
- [50] I.P. Morton, and M.F. Lewis, "Effect of iron impurities on the thermal conductivity of magnesium oxide single crystals below room temperature", Physical Review B, Vol 3, 552, 1971.

